Monthly Notices of the ROYAL ASTRONOMICAL SOCIETY
MNRAS **515,** 1871–1896 (2022) https://doi.org/10.1093/mnras/stac1771

Radio fossils, relics, and haloes in Abell 3266: cluster archaeology with ASKAP-EMU and the ATCA

C. J. Riseley [1,2,3★] E. Bonnassieux,[1,2] T. Vernstrom [3,4] T. J. Galvin [3,5] A. Chokshi [6,7,8] A. Botteon [9] K. Rajpurohit [1,2] S. W. Duchesne [3,5] A. Bonafede,[1,2] L. Rudnick [10] M. Hoeft [11] B. Quici,[5] D. Eckert,[12] M. Brienza,[1,2] C. Tasse,[13,14] E. Carretti [2] J. D. Collier,[3,15,16] J. M. Diego [17] L. Di Mascolo,[18,19,20] A. M. Hopkins,[21] M. Johnston-Hollitt,[22] R. R. Keel,[5] B. S. Koribalski [8,16] and T. H. Reiprich[23]

Affiliations are listed at the end of the paper

Accepted 2022 June 20. Received 2022 June 13; in original form 2022 May 4

ABSTRACT

Abell 3266 is a massive and complex merging galaxy cluster that exhibits significant substructure. We present new, highly sensitive radio continuum observations of Abell 3266 performed with the Australian Square Kilometre Array Pathfinder (0.8–1.1 GHz) and the Australia Telescope Compact Array (1.1–3.1 GHz). These deep observations provide new insights into recently reported diffuse non-thermal phenomena associated with the intracluster medium, including a 'wrong-way' relic, a fossil plasma source, and an as-yet unclassified central diffuse ridge, which we reveal comprises the brightest part of a large-scale radio halo detected here for the first time. The 'wrong-way' relic is highly atypical of its kind: it exhibits many classical signatures of a shock-related radio relic, while at the same time exhibiting strong spectral steepening. While radio relics are generally consistent with a quasi-stationary shock scenario, the 'wrong-way' relic is not. We study the spectral properties of the fossil plasma source; it exhibits an ultrasteep and highly curved radio spectrum, indicating an extremely aged electron population. The larger scale radio halo fills much of the cluster centre, and presents a strong connection between the thermal and non-thermal components of the intracluster medium, along with evidence of substructure. Whether the central diffuse ridge is simply a brighter component of the halo, or a mini-halo, remains an open question. Finally, we study the morphological and spectral properties of the multiple complex radio galaxies in this cluster in unprecedented detail, tracing their evolutionary history.

Key words: galaxies: clusters: general – galaxies: clusters: individual: Abell 3266 – galaxies: clusters: intracluster medium – X-rays: galaxies: clusters.

1 INTRODUCTION

Residing at the intersections of the large-scale structure of the Universe's Cosmic Web, galaxy clusters are some of the largest gravitationally bound objects in the Universe. Around ∼80 per cent of the mass of a galaxy cluster is comprised of dark matter, with the remaining ∼20 per cent being baryonic matter. The dominant contribution to this baryonic matter content of a cluster is the intracluster medium (ICM), a hot ($T \sim 10^7$–10^8 K), tenuous ($n_e \sim 10^{-3}$ cm^{-3}) plasma that emits via the bremsstrahlung mechanism at X-ray wavelengths and scatters photons of the cosmic microwave background (CMB) via the Sunyaev–Zeldovich effect.

In the hierarchical model of structure formation, galaxy clusters grow through a variety of processes, including accretion of material from the external medium, absorption of individual galaxies and groups, and major merger events. Major mergers are some of the most dramatic events since the big bang, depositing tremendous quantities of energy (∼10^{64} erg; Ferrari et al. 2008) into the ICM in the form of shocks and turbulence.

Spectacular sources of diffuse radio emission have been detected in many merging clusters (for a recent observational review, see van Weeren et al. 2019). These sources of diffuse emission fall broadly into three categories: radio relics, radio haloes, and mini-haloes. However, new and highly sensitive low-frequency radio observations have revealed that the picture is much more complex, and other types of diffuse source (many of which do not fit our taxonomy) have been detected in recent years (e.g. Govoni et al. 2019; Botteon et al. 2020a,c; Ignesti et al. 2020b; Hodgson et al. 2021; Knowles et al. 2022; Venturi et al. 2022). The extremely large spatial scale of these sources, combined with the short lifetime of the relativistic electrons generating the synchrotron emission ($\tau \lesssim 10^8$ yr) implies *in situ* acceleration by physical processes in the ICM.

Radio relics are extended synchrotron sources (typically megaparsec-scale) that are usually located towards the cluster outskirts. When imaged at sufficiently high resolution, relics frequently show significant filamentary substructure (for example Owen et al. 2014; van Weeren et al. 2017b; Di Gennaro et al. 2018; Rajpurohit

★ E-mail: christopher.riseley@unibo.it

et al. 2018, 2020; Botteon et al. 2020c; de Gasperin et al. 2022). Relics also frequently exhibit a high linear polarisation fraction, with magnetic field vectors aligned with the long axis of the relic, presumably tracing shock compression of magnetic fields (e.g. Bonafede et al. 2012; Riseley et al. 2015; Loi et al. 2020; Rajpurohit et al. 2021b; de Gasperin et al. 2022).

Relics are generally believed to be associated with shocks induced by merger events, and indeed a growing number of clusters show associations between relics and shocks detected at X-ray wavelengths (Finoguenov et al. 2010; Shimwell et al. 2015; Botteon et al. 2016b). It is commonly accepted that the mechanism responsible for deposition of shock energy into the ICM is some form of diffusive shock acceleration (DSA; Ensslin et al. 1998; Roettiger, Burns & Stone 1999). However, one of the open questions is the origin of the cosmic-ray electron (CRe) population that gives rise to the synchrotron emission.

Specifically, the most active area of debate is whether the CRe population originates from the thermal pool (Hoeft & Brüggen 2007) or from a pre-existing population of mildly relativistic electrons (Kang & Ryu 2011), which is frequently referred to as the 're-acceleration' scenario. Indeed, a growing number of radio relics have been found that appear to show connections with cluster-member radio galaxies, providing support for the re-acceleration scenario (van Weeren et al. 2017a; Stuardi et al. 2019; HyeongHan et al. 2020; Jones et al. 2021).

While 'standard' DSA from the thermal pool can successfully recreate many observed properties of radio relics, some major difficulties remain. In the case of weak shocks, DSA requires an unphysically large acceleration efficiency to reproduce the most luminous radio relics (Botteon et al. 2020b). Additionally, the Mach numbers derived from X-ray observations are frequently found to be lower than those derived from radio observations. However, recent simulations of cluster mergers can go some way to reconciling this discrepancy between radio-derived and X-ray-derived Mach numbers, depending on the system geometry (Hong, Kang & Ryu 2015; Dominguez-Fernandez et al. 2021; Wittor et al. 2021). Furthermore, the theoretical framework of the multishock scenario – whereby an existing electron population is re-accelerated by repeated shocks – is now being explored (Kang 2021; Inchingolo et al. 2022). The CRe population generated by this scenario shows significantly higher luminosity than that of a CRe population that has been shocked only a single time; in addition, the multishock CRe population shows a spectral energy distribution (SED) that clearly departs from a single power-law behaviour.

Radio haloes are centrally located, largely amorphous, megaparsec-scale synchrotron sources that usually exhibit negligible polarisation fraction. The synchrotron emission from haloes generally follows the distribution of the thermal ICM (as traced by X-ray emission), implying a direct connection between thermal and non-thermal components in the ICM (see Feretti et al. 2001; Govoni et al. 2001a,b; Giovannini et al. 2009; Boschin, Girardi & Barrena 2012; Shimwell et al. 2014; Cantwell et al. 2016; Bruno et al. 2021; Rajpurohit et al. 2021a,b; de Gasperin et al. 2022).

The more commonly accepted scenario for generation of radio haloes involves the acceleration of CRe through turbulence injected into the ICM following merger events (Brunetti et al. 2001; Petrosian 2001). The turbulent (re-)acceleration scenario naturally links the presence of radio haloes with ongoing cluster mergers, and successfully explains many of the observed halo properties, such as the existence of ultrasteep spectrum radio haloes (e.g. Brunetti et al. 2008).

One alternative to the turbulent (re-)acceleration scenario is the secondary (or hadronic) scenario, whereby CRe are injected throughout the ICM via inelastic collisions between cosmic-ray protons (CRp) and thermal protons of the ICM (Dennison 1980; Blasi & Colafrancesco 1999). However, purely hadronic scenarios cannot work for radio haloes: even the recent claim of a gamma-ray detection towards the Coma cluster (Xi et al. 2018), if attributed *entirely* to hadronic collisions in the ICM, only accounts for up to 20 per cent of the observed radio halo luminosity (Adam et al. 2021).

Finally, mini-haloes remain the most poorly understood class, as only some 32 are currently known, compared to around 100 radio relics and a similar number of radio haloes (van Weeren et al. 2019). Mini-haloes are moderately extended (typically around 0.1–0.3 Mpc) objects that are centrally located in relaxed clusters that also host a powerful radio source associated with the brightest cluster galaxy (BCG).

Although it remains an active area of theoretical discussion, two principal formation mechanisms exist for mini-haloes: either turbulent (re-)acceleration (Gitti, Brunetti & Setti 2002; ZuHone et al. 2013, 2015) or hadronic processes (Pfrommer & Enßlin 2004). Under the former scenario, mini-haloes are generated by synchrotron radiation from CRe (possibly injected by the BCG radio counterpart as well as other cluster-member radio galaxies) that have been (re-)accelerated to relativistic energies by minor/off-axis merger events, core sloshing within the cool core and/or gas dynamics driven by cold fronts (see for example Gitti et al. 2002; ZuHone et al. 2013; Brunetti & Jones 2014). However, any minor merger event would have to generate large-scale bulk motions of gas while leaving the cool core intact (ZuHone et al. 2015).

The hadronic scenario is much the same as that for radio haloes: that mini-haloes are generated by relativistic electrons formed through collisions between CRp and thermal protons of the ICM. While tensions with limits from *Fermi* also exist for mini-haloes, recent work by Ignesti et al. (2020a) showed that the limits do not completely exclude the hadronic scenario. Recent multifrequency observations of mini-haloes have shown that our understanding of their underlying physics is far from complete, with multicomponent mini-haloes being found in increasing numbers (Savini et al. 2018, 2019; Raja et al. 2020; Biava et al. 2021; Riseley et al. 2022). In many of these cases, both the turbulent and hadronic mechanisms can explain some of the observational evidence, but neither scenario is able to explain all physical properties, and thus further work is required to understand the detailed and complex physical processes at work.

As well as these classes of diffuse synchrotron emission that originate with physical processes in the ICM, many clusters also host embedded resolved radio galaxies that exhibit a range of morphologies. We will collectively refer to these sources as 'bent-tailed radio galaxies' as further subcategorisation – such as the canonical wide-angle-tail (WAT), narrow-angle-tail (NAT), and head-tail (HT) classifications – is highly subjective and strongly affected by a number of observational systematics (such as projection effects).

The morphological and spectropolarimetric properties of bent-tailed radio galaxies provide powerful probes of the cluster weather, as well as thermal and non-thermal components in the ICM (e.g. Burns 1998; Pratley et al. 2013; Johnston-Hollitt, Dehghan & Pratley 2015; Gendron-Marsolais et al. 2020, 2021; Lal 2020; Brienza et al. 2021). For example, turbulence, cluster winds, bulk motions, and/or the relative motion of these galaxies can all result in a variety of different observed morphologies.

Remnant radio galaxies (also known as 'dying' or 'fossil' radio sources) represent the end phase of radio galaxy evolution. These

sources comprise aged plasma left behind by an active galaxy after its central engine has switched off. Following standard synchrotron ageing processes, these sources fade more rapidly towards higher frequencies, becoming detectable only at increasingly long wavelengths before fading altogether (e.g. Murgia et al. 2011; Harwood et al. 2013; Harwood, Hardcastle & Croston 2015; Brienza et al. 2016; Godfrey, Morganti & Brienza 2017; Turner 2018; Turner et al. 2018; Quici et al. 2022).

With the advent of the next-generation long-wavelength interferometers such as the LOw-Frequency ARray (LOFAR; van Haarlem et al. 2013) and the Murchison Widefield Array (MWA; Tingay et al. 2013; Wayth et al. 2018), our understanding of fossil plasma sources is increasing. However, despite them being studied in increasing numbers (e.g. Brienza et al. 2017, 2021, 2022; Mahatma et al. 2018; Duchesne & Johnston-Hollitt 2019; Randriamanakoto, Ishwara-Chandra & Taylor 2020; Hodgson et al. 2021; Jurlin et al. 2021; Knowles et al. 2022), they remain a relatively rare and short-lived phase of radio galaxy evolution, comprising some ∼5–15 per cent of the radio galaxy population.

1.1 Abell 3266

Situated at (J2000 Right Ascension, Declination) = ($04^{h}31^{m}24\overset{s}{.}1$, $-61^{d}26^{m}38^{s}$), Abell 3266 (also known as Sersic 40−6) is a nearby cluster of galaxies at redshift $z = 0.0594$ (Quintana, Ramirez & Way 1996). With a total mass of $(6.64^{+0.11}_{-0.12}) \times 10^{14}$ $M_{\odot}$ (Planck Collaboration XXVII 2016), it is the most massive member of the Horologium-Reticulum supercluster (Fleenor et al. 2005).

Abell 3266 has been extensively observed at X-ray wavelengths (Markevitch et al. 1998; De Grandi & Molendi 1999; Mohr, Mathiesen & Evrard 1999; Henriksen, Donnelly & Davis 2000; Sauvageot, Belsole & Pratt 2005; Finoguenov et al. 2006; Sanders et al. 2022). All observational results show that Abell 3266 is undergoing a complex merger event, presenting an elongated and asymmetric X-ray surface brightness distribution, as well as an asymmetric temperature profile. Most recently, Sanders et al. (2022) reported a detailed X-ray analysis of Abell 3266 using new data from the eROSITA telescope (Predehl et al. 2021) on board the *Spectrum Röntgen Gamma* (*SRG*) satellite. eROSITA revealed much substructure within the cluster, including two weak (Mach number $\mathcal{M} \sim 1.5$–1.7) shock fronts towards the cluster periphery at a distance of around 1.1 Mpc from the cluster centre.

Detailed optical observations presented by Dehghan et al. (2017) have revealed that the cluster contains some ∼800 member galaxies, distributed between two subclusters and at least six subgroups (which lie predominantly to the north and NW of the cluster centre). Overall, Abell 3266 exhibits a significant velocity dispersion of $v_{\rm d} \sim 1400$ km s^{-1} (Dehghan et al. 2017), although those authors note that this is likely due to the relative motions of the various subclusters and subgroups comprising this complex system. The BCG exhibits a dumbbell morphology and shows strong tidal distortion, likely arising as a result of the merger between the two main subclusters (Henriksen et al. 2000; Henriksen & Tittley 2002).

Despite the extensive X-ray and optical coverage, there is a comparative lack of detailed radio observations. Most historic studies have been performed with either narrow-band instruments (Murphy 1999; Reid 1999; Murphy & Hunstead 2002) or low-resolution radio telescopes (Bernardi et al. 2016; Riseley 2016). Analysis of narrow-band observations performed with the Australia Telescope Compact Array (ATCA; Frater, Brooks & Whiteoak 1992) reveals the cluster is host to several spectacular tailed radio galaxies as well as a number of compact and diffuse sources (Murphy 1999; Reid 1999; Dehghan 2014). One of the extended sources, situated to the NW of the cluster centre, shows an elongated morphology and possesses a steep spectrum between 1.4 GHz and 843 MHz. When viewed in concert with a potential optically selected host galaxy, the interpretation was that this elongated radio source is perhaps a remnant radio galaxy (Murphy 1999) or a radio relic (Dehghan 2014).

Abell 3266 was observed with MeerKAT as one of the X-ray selected clusters in the MeerKAT Galaxy Cluster Legacy Survey (GCLS; Knowles et al. 2022), under the identifier J0431.4−6126. These observations have been used to study the resolved nature of the aforementioned complex radio galaxy, detecting a variety of features not seen before in this source. For highlights, see Knowles et al. (2022); for a detailed discussion and interpretation of the features seen in this source, see Rudnick et al. (2021). Knowles et al. (2022) also report the first clear detection of a radio relic in Abell 3266, although Murphy (1999) reported a tentative identification at around 2.5σ significance.

Duchesne et al. (2022) present the first low-frequency observations of Abell 3266 using the Phase II MWA (Wayth et al. 2018), covering the frequency range 88–216 MHz. These observations confirm the detection of the radio relic, as well as revealing two ultrasteep-spectrum fossil plasma sources in the ICM of Abell 3266. However, while Abell 3266 bears many of the typical characteristics of clusters that host a radio halo, the deep MWA observations presented by Duchesne et al. (2022) do not detect a halo. By injecting simulated haloes with a variety of spatial scales and luminosities, Duchesne et al. demonstrate that any halo that is present but undetected would lie up to a factor five below established scaling relations between cluster mass and radio halo power (e.g. Cassano et al. 2013; Duchesne, Johnston-Hollitt & Wilber 2021c).

This paper presents analysis of new, deep, broad-band radio data from the ATCA and the Australian Square Kilometre Array Pathfinder (ASKAP; Johnston et al. 2007; DeBoer et al. 2009; Hotan et al. 2021), in conjunction with ancillary X-ray data from *XMM–Newton*. These observations were performed independently of the MeerKAT GCLS data release; the results are very complementary and allow us to gain new and detailed insights into this rich, complex cluster. We present our showcase multiwavelength image of Abell 3266 in Fig. 1.

The remainder of this paper is divided as follows: we discuss the observations and data reduction in Section 2, and present our results in Section 3. In Section 4, we discuss our new results on diffuse radio sources in Abell 3266, and in Section 5, we discuss selected tailed radio galaxies. We draw our conclusions in Section 6. Throughout this work, we take the redshift of Abell 3266 to be $z = 0.0594$ (Quintana et al. 1996). We assume a ΛCDM cosmology of $H_0 = 73$ km s^{-1} Mpc^{-1}, $\Omega_{\rm m} = 0.27$, $\Omega_{\Lambda} = 0.73$. With this cosmology, at the redshift of Abell 3266, an angular distance of 1 arcsec corresponds to a physical distance of 0.906 kpc. We adopt the convention that flux density S is proportional to observing frequency ν as $S \propto \nu^{\alpha}$, where α is the spectral index, and all uncertainties are quoted at the 1σ level.

2 OBSERVATIONS AND DATA REDUCTION

2.1 Australia Telescope Compact Array

We observed Abell 3266 with the ATCA between 2020 October and 2021 October, for a total of approximately 66 h (project ID C3389, P.I. Riseley). Observations were performed using the Compact Array Broad-band Backend (CABB; Wilson et al. 2011) in the 16-cm

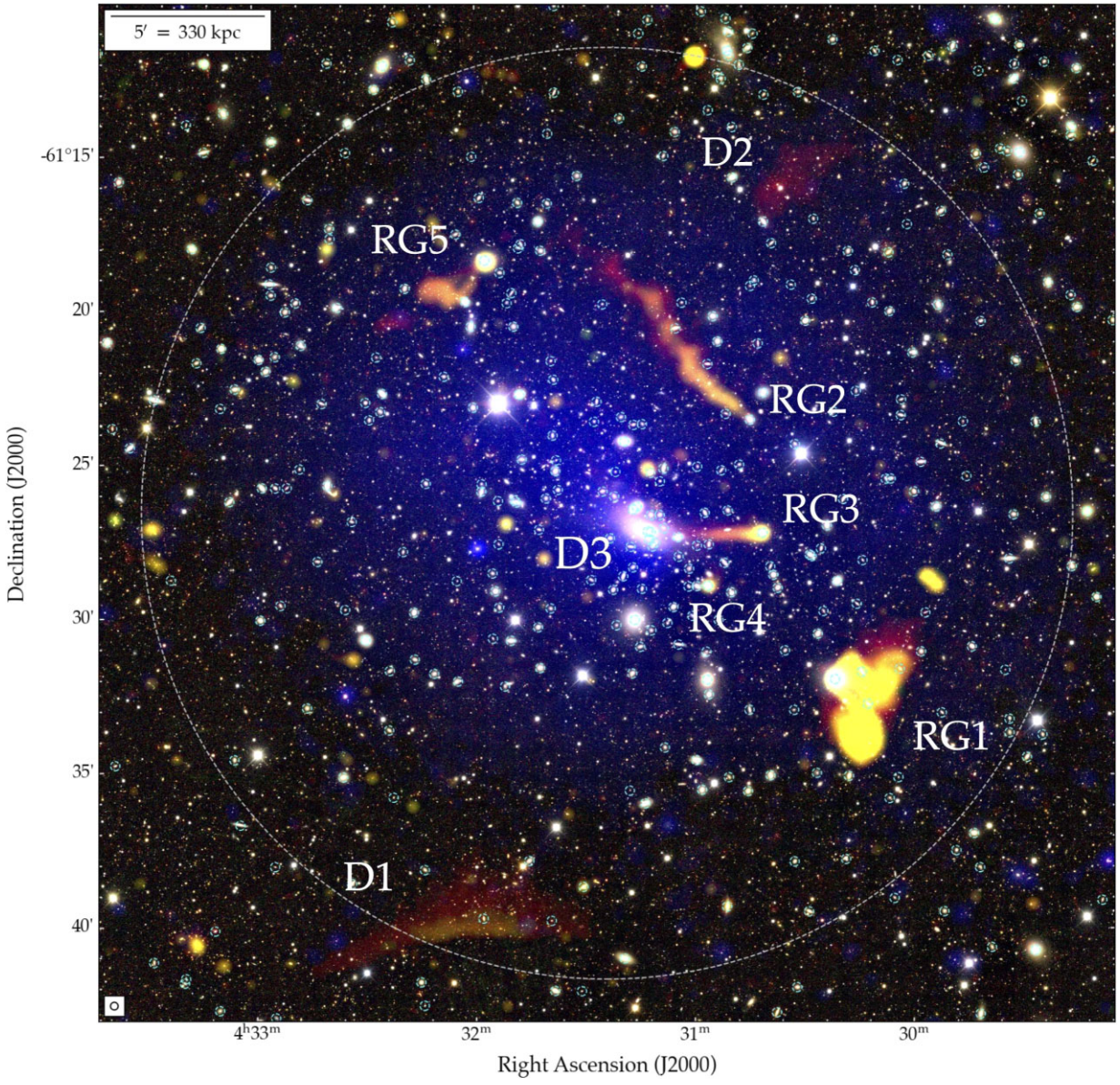

Figure 1. Colour-composite image of Abell 3266, overlaying radio colour on optical RGB. Optical RGB image comprises *i*, *r*, and *g* bands from Data Release 2 of the Dark Energy Survey (DES). We overlay the radio surface brightness measured by ASKAP (943 MHz; red channel) and the ATCA (2.1 GHz; green channel), both at 15-arcsec resolution. Also overlaid is the [0.5–2 keV] X-ray surface brightness measured by *XMM–Newton* (blue channel). Dashed cyan circles indicate cluster-member radio galaxies identified by Dehghan et al. (2017). The dashed silver circle indicates a 1-Mpc radius from the cluster centre, given our cosmology. Labels identify sources of interest to be discussed later, with 'D' indicating that a source's nature is 'diffuse', and 'RG' indicating that it is an active radio galaxy.

band, which covers the frequency range 1.1–3.1 GHz at a spectral resolution of 1 MHz.

Four complementary array configurations were used, with baselines between 30 m and 6 km in length, providing sensitivity to a broad range of angular scales and a nominal resolution of around 6 arcsec. We covered Abell 3266 using a mosaic of four pointings, spaced at 50 per cent of the primary beam (PB) full width at half-maximum (FWHM), in order to ensure that the entire cluster volume could be probed in full polarization while minimizing the effects of off-axis instrumental leakage. This paper presents our continuum results; polarisation data will be presented in a future paper. Our observations are summarized in Table 1.

Table 1. ATCA observations of Abell 3266.

Date	Start time (AEST)	Hours observed	Array configuration
2020 Oct 24	19:30	14	6B
2020 Oct 25	19:30	14	6B
2020 Dec 18	17:00	14	1.5A
2020 Dec 20	21:30	6	1.5A
2021 Jan 26	14:30	12	EW352
2021 Oct 10	17:30	5.5	H168

Our flux density scale was set using a 10–15 min scan of PKS B1934−638 on each day. We applied standard calibration and radio frequency interference (RFI) flagging techniques using the MIRIAD software package (Sault, Teuben & Wright 1995). A total of around 40 per cent of the data were flagged due to the presence of strong RFI, which dominates specific channel ranges and occurs primarily at the low-frequency end of the band.

All imaging was carried out using the DDFACET software package (Tasse et al. 2018). We employed `robust = 0` weighting (Briggs 1995) to strike a balance between sensitivity and resolution. As Abell 3266 hosts a variety of extended radio sources, we used the subspace deconvolution (SSD; Tasse et al. 2018) algorithm in order to more correctly model this diffuse radio emission.

Self-calibration was performed using the KILLMS software package (Tasse 2014; Smirnov & Tasse 2015). Initial self-calibration was carried out in direction-independent (DI) mode; four rounds of phase-only self-calibration were performed, followed by three rounds of amplitude & phase self-calibration. All four pointings were jointly deconvolved using new functionality incorporated into the `dev` version of DDFACET for this project, including implementation of the ATCA 16 cm band beam model.[1]

We used the quality-based weighting scheme developed by Bonnassieux et al. (2018) to weight our calibration solutions throughout our self-calibration process. This weighting scheme uses the gain statistics (which are used within the calibration solver to find optimal gain solutions) to estimate the relative quality of each gain solution, and weighs the corrected visibilities appropriately. After each solve, KILLMS computes these weights by default, as minimal computational overhead is required. Typically, the usage of this weighting scheme results in faster convergence of the self-calibration process.

After seven rounds of DI self-calibration, our solutions had largely converged, and we then inspected our mosaic for residual direction-dependent (DD) errors. While the quality of our jointly deconvolved mosaic was generally high, some of the brighter sources in Abell 3266 showed residual DD errors, limiting our overall dynamic range. We tessellated the sky into twelve clusters, and performed several rounds of DD self-calibration and imaging, solving for gains in both amplitude and phase and refining our solutions with each iteration. Once our DD self-calibration had suitably converged, we proceeded to generate our final science images. The native resolution of our `robust = 0` ATCA mosaic is around 4.5 arcsec; to match the resolution of our ASKAP mosaics, we generated our science images at 9- and 15-arcsec resolution by varying the `robust` parameter appropriately (`robust = 0` for our 9-arcsec image, `robust = +0.7` for our 15-arcsec image) before convolving with an elliptical Gaussian to achieve the desired resolution. We adopt a representative 5 per cent calibration uncertainty in our ATCA mosaic of Abell 3266. The right-hand panel of Fig. 2 shows our 6-arcsec ATCA image of Abell 3266; Fig. A1 of the supplementary material illustrates the dramatic improvement in image fidelity enabled by applying these next-generation algorithms to ATCA data processing.

2.2 Australian Square Kilometre Array Pathfinder

ASKAP comprises 36 12-m dishes located in the Murchison Radioastronomy Observatory (MRO) in Western Australia, observing between 700 MHz and 1.8 GHz, with an instantaneous bandwidth of up to 288 MHz. Due to the unique phased-array feed (PAF; Hotan et al. 2014; McConnell et al. 2016) technology, ASKAP is capable of simultaneously forming up to 36 independent beams, covering some $\sim$30 deg^2, making ASKAP a powerful survey telescope.

With this large field of view (FOV), operating at low frequencies, and with baselines in the range 22 m and 6 km (providing sensitivity to radio emission on a wide range of angular scales), ASKAP is ideally suited to observations of low-surface-brightness diffuse radio sources typically found in many clusters of galaxies (HyeongHan et al. 2020; Wilber et al. 2020; Brüggen et al. 2021; Di Mascolo et al. 2021; Duchesne et al. 2021a,c; Venturi et al. 2022).

Abell 3266 was observed with ASKAP during Early Science operations for the Evolutionary Map of the Universe (EMU; Norris et al. 2011) survey, under SBID 10636. Observations were performed on 2019 November 24, for a total on-source time of approximately seven hours. These observations were performed with 34 antennas, as two (ak09, ak32) did not participate in the observing run. The field was observed in Band 1 at a central frequency of 943 MHz, with a bandwidth of 288 MHz. Our target was observed using the 'closepack-36' beam configuration, covering a total FOV of around 30 deg^2.

PKS B1934−638 is routinely used by ASKAP for bandpass calibration and absolute flux density scale calibration, and is observed daily on a per-beam basis. Initial data processing was performed using the ASKAPSOFT pipeline (Guzman et al. 2019), which incorporates RFI flagging, bandpass calibration, averaging and multiple rounds of DI amplitude and phase self-calibration.[2] Each beam is processed independently before being co-added in the image plane. Following pipeline processing, the data were averaged to 1 MHz spectral resolution. Aside from the two missing antennas, around 15 per cent of the data were flagged by the ASKAPSOFT pipeline.

The mosaic has a common resolution of 15.5 × 13.7 arcsec^2, with an off-source rms noise of 33 μJy beam^{-1} in the vicinity of Abell 3266. In general, the quality of the full ASKAP mosaic covering the Abell 3266 field was very high. However, residual DD errors remain in the mosaic – particularly evident in regions around relatively bright sources ($S \gtrsim 1$ Jy). As such, we opted to perform postprocessing using DDFACET and KILLMS.

Abell 3266 was principally covered by two beams (Beam 15 and Beam 20) from the ASKAP mosaic. As such, we retrieved the calibrated visibilities for these beams via the CSIRO[3] ASKAP Science Data Archive (CASDA[4]; Chapman et al. 2017; Huynh et al. 2020). These beams were processed independently, and mosaicked in the image plane after performing further self-calibration.

For each beam, we imaged an area of 3 × 3 deg^2, in order to include particularly bright sources in the wide field. Imaging was performed in a similar manner to our ATCA data, using DDF with the SSD algorithm. We performed a single round of DI self-calibration, before switching to the DD regime. The sky was tessellated into nine clusters, and we performed two rounds of amplitude-and-phase self-calibration and imaging on each beam.

To correct for PB attenuation, we followed the same principles applied by Wilber et al. (2020). We assume a Gaussian PB with a FWHM of the form FWHM $= 1.09\lambda/D$, where $D = 12$ m is the antenna diameter, and $\lambda = 0.3179$ m is the wavelength at our reference frequency (943 MHz). We linearly mosaicked our final

[1] See https://www.narrabri.atnf.csiro.au/people/ste616/beamshapes/beamshape_16cm.html for details of the ATCA 16-cm band beam model.

[2] https://www.atnf.csiro.au/computing/software/askapsoft/sdp/docs/current/pipelines/introduction.html.

[3] Commonwealth Scientific & Industrial Research Organisation.

[4] https://research.csiro.au/casda/.

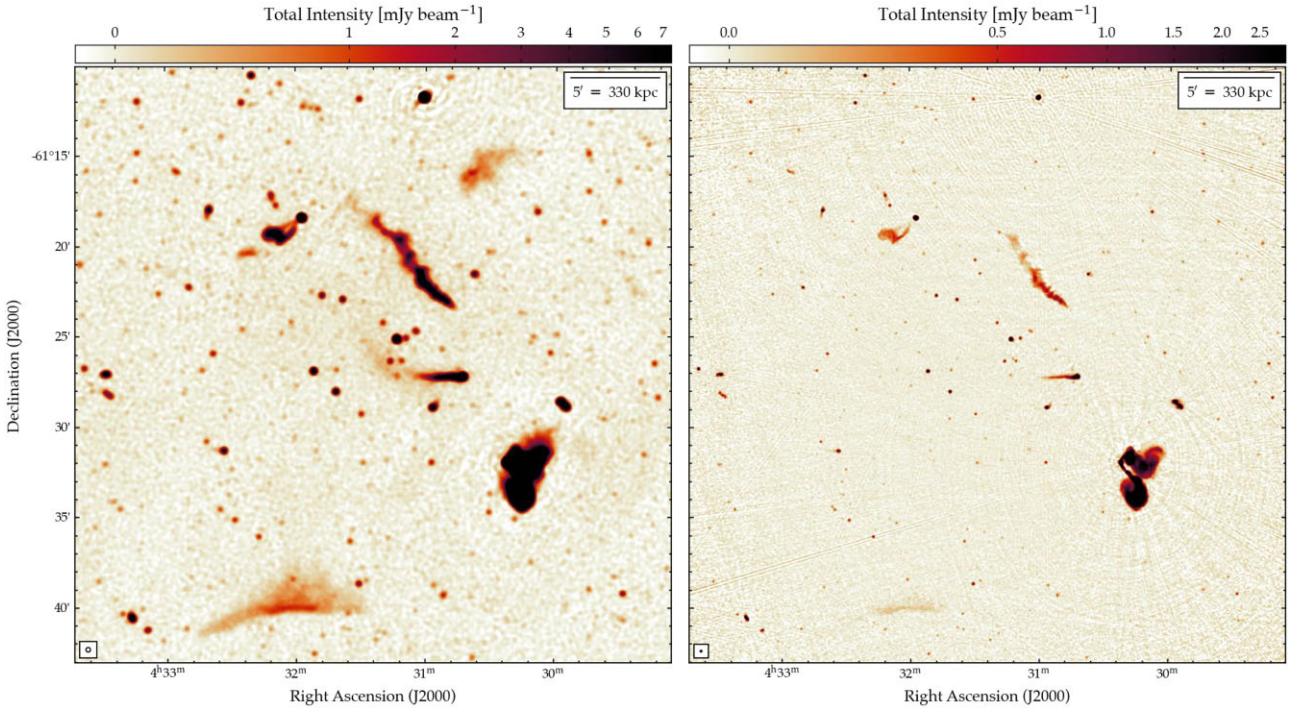

Figure 2. Example radio images of Abell 3266, as observed with ASKAP (left-hand panel; 943 MHz) and the ATCA (right-hand panel; 2.1 GHz). Colour maps range from -3σ to 200σ on an arcsinh stretch, to emphasize faint, diffuse emission. The typical off-source noise is 36.7 μJy beam^{-1} in our ASKAP image (15-arcsec resolution), and 14.5 μJy beam^{-1} in our ATCA image (6-arcsec resolution).

DD-calibrated images of our two selected ASKAP beams, weighted according to the PB response, and applied a factor of 2 to account for the difference between the Stokes *I* convention adopted by ASKAP and other imaging software. We also applied a bootstrap factor of 1.075 to our ASKAP data, as suggested by the CASDA validation report; as such, we adopt a conservative 10 per cent calibration uncertainty in our ASKAP maps of Abell 3266.

We show our final ASKAP image of Abell 3266 at 15-arcsec resolution in the left-hand panel of Fig. 2. We also demonstrate the significant improvement in image fidelity that is enabled by applying KILLMS and DDFACET to ASKAP data in Fig. A2 of the supplementary material. We note that the majority of the large-scale 'diffuse flux' in the left-hand panel of Fig. A2 is a manifestation of calibration errors associated with the DI processing of these data. The significant suppression in these artefacts brought about by DD calibration and our use of SSD-clean is evident in the right-hand panel of Fig. A2.

2.3 *XMM–Newton*

We retrieved from the *XMM–Newton* Science Archive[5] the 13 observations on Abell 3266 that are listed in Table 2. These data were collected in three different epochs: ObsIDs 0105260701–0105262201 in 2000, ObsID 0105262501 in 2003, and ObsIDs 0823650301–0823650701 in 2018. While the earliest observations cover the central region of the cluster and were originally presented by Sauvageot et al. (2005) and Finoguenov et al. (2006), the latest observations cover the virial radius region and were carried out in the context of the *XMM–Newton* Cluster Outskirts Project (X-COP; Eckert et al. 2017). We processed the data using the *XMM–Newton* Scientific Analysis System (SAS v16.1.0) and the Extended Source Analysis Software (ESAS) data reduction scheme (Snowden et al. 2008) following the working flow described by Ghirardini et al. (2019). The final clean exposure for each ObsID and for each detector of the European Photon Imaging Camera (EPIC) is summarized in Table 2. We then combined the count images and corresponding exposure images of each data set to produce a mosaic exposure-corrected image in the 0.5–2.0 keV band that was used to compare the distribution of the synchrotron diffuse cluster sources with respect to the thermal ICM.

Table 2. *XMM–Newton* observations of Abell 3266.

ObsID	Target	Clean exposure time (ks)		
		MOS1	MOS2	pn
0105260701	A3266_f1	19.0	19.3	15.5
0105260801	A3266_f2	19.7	19.7	15.5
0105260901	A3266_f3	23.4	23.0	17.9
0105261001	A3266_f4	2.8	2.8	0.5
0105261101	A3266_f5	11.6	12.1	7.1
0105262001	A3266_f6	6.2	5.7	2.5
0105262101	A3266_f5	5.6	6.2	2.5
0105262201	A3266_f4	2.9	2.9	3.2
0105262501	A3266_f6	6.2	6.9	3.2
0823650301	A3266NW	22.3	22.9	10.4
0823650401	A3266NE	24.3	26.0	16.1
0823650601	A3266SW	24.2	25.4	20.2
0823650701	A3266NW	31.2	32.8	20.3

[5]http://nxsa.esac.esa.int/nxsa-web.

Table 3. Summary of image properties for our maps of Abell 3266.

Image	Imaging `robust`	RMS noise (μJy beam^{-1})	Resolution (arcsec)	LAS (arcmin)
ASKAP	−1.5	36.7	15	48
	−2.0	90.9	9	
ATCA	+0.7	13.9	15	16
	+0.0	13.7	9	

Note. 'LAS' denotes the theoretical largest recoverable angular scale of each image.

3 RESULTS

Fig. 1 presents our 'showcase' colour-composite image of Abell 3266, with radio colour overlaid on an optical RGB image constructed from Data Release 2 (DR2) of the DES (DES Collaboration et al. 2021). The optical RGB image uses DES *i*, *r*, and *g* bands in the respective channels. The radio surface brightnesses measured from ASKAP and ATCA maps (both at 15-arcsec resolution) are inserted in the red and green channels, respectively. Finally, we show the X-ray surface brightness measured by *XMM–Newton*, smoothed using a Gaussian filter with a 7 pixel FWHM, in the blue channel. In this image, typical synchrotron emission ($\alpha \sim -0.8$) exhibits a yellow hue, with steep-spectrum emission appearing redder in colour. Conversely, flat-spectrum sources appear green in colour.

We also present example radio maps in Fig. 2. The ASKAP image shown in Fig. 2 has an rms noise of 36.7 μJy beam^{-1} at a resolution of 15 arcsec and a reference frequency of 943 MHz. The ATCA image displayed in Fig. 2 has an rms noise of 14.5 μJy beam^{-1} at a resolution of 6 arcsec and a reference frequency of 2.1 GHz.

Our new observations reveal a plethora of spectacular tailed radio galaxies along with three diffuse sources, the nature of which is not immediately obvious. All analysis detailed later in this paper is performed on matched-resolution images at 9 and 15 arcsec. We opted to study the radio properties of the cluster at two different resolutions in order to better recover the spatially resolved properties of the complex cluster-member radio galaxies (by using our 9-arcsec-resolution images) and improve our signal-to-noise ratio (S/N) when studying the diffuse, steep-spectrum non-thermal sources (using our 15-arcsec-resolution images). All image properties (such as rms noise and resolution) are summarized in Table 3.

4 DIFFUSE RADIO SOURCES

Throughout this analysis, we draw predominantly on the ASKAP and ATCA images presented in this work. Where appropriate, we incorporate flux density measurements from the MWA-2 data presented by Duchesne et al. (2022). We also incorporate data products from MeerKAT images of Abell 3266 from the recent first data release from the MeerKAT GCLS (Knowles et al. 2022). These data products have not been corrected for DD effects, and as such the image fidelity and dynamic range varies with frequency; this is principally visible at the lower end of the MeerKAT band, where a bright off-axis radio source far to the south-west of Abell 3266 causes artefacts that underlay much of the cluster.[6] However, at frequencies above around 1 GHz, these effects become increasingly suppressed due to the narrowing PB FWHM. As such, we extracted images at frequencies of 1043, 1092, 1312, 1381, 1448, 1520, and 1656 MHz from the MeerKAT GCLS 15-arcsec-resolution cube, and incorporated these into our analysis. We assume a representative 10 per cent calibration uncertainty for all MeerKAT measurements incorporated in our analysis.

[6]This source was also problematic for the DI-calibrated ASKAP mosaic; after DD-calibration, the impact of this far-field source on our mosaic is negligible.

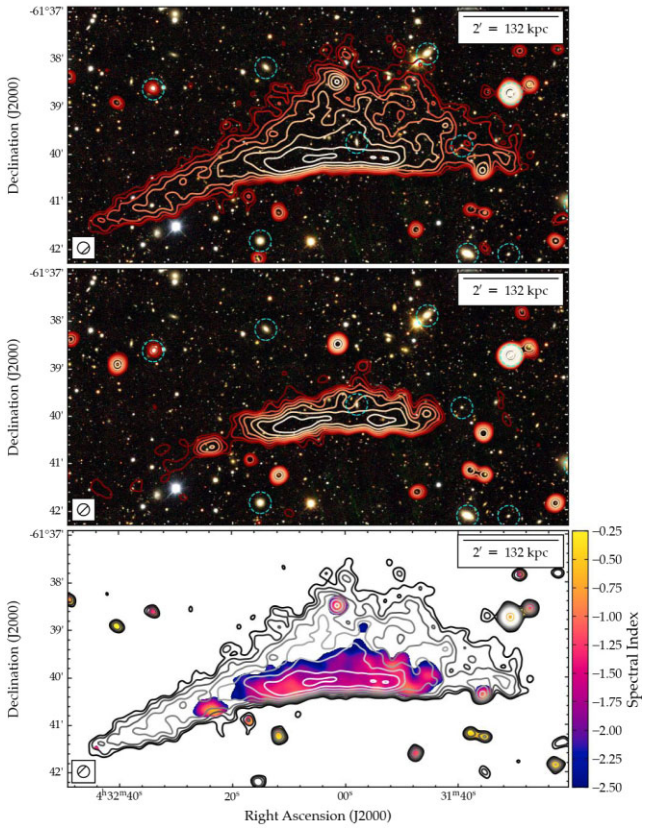

Figure 3. Radio-on-optical overlay of the 'wrong-way' relic to the SE of Abell 3266. Contours show the surface brightness measured by ASKAP (943 MHz; upper panel) and the ATCA (2.1 GHz; middle panel) in our 15-arcsec images. The colourmap shows our optical RGB image from DES, as per Fig. 1. Dashed cyan circles denote cluster-member galaxies identified by Dehghan et al. (2017). The lower panel presents the spectral index map between 943 MHz and 2.1 GHz at 15-arcsec resolution. Contours show the ASKAP surface brightness. In each panel, contours start at 3σ and scale by a factor of $\sqrt{2}$, and the hatched circle in the lower left-hand corner indicates the restoring beam size (15 arcsec).

4.1 Source D1: a 'wrong-way' relic

This source lies at a projected distance of 15.8 arcmin ($\sim$1.04 Mpc) to the SE of the cluster centre. Source D1 is a highly extended, asymmetric diffuse radio source – in this case, a radio relic. This relic was tentatively identified by Murphy (1999) at around 2.5σ significance; the first unambiguous detection was recently reported by Knowles et al. (2022), and the low-frequency properties first explored by Duchesne et al. (2022). Fig. 3 presents radio surface brightness contours of this source from our 15-arcsec-resolution ASKAP (upper panel) and ATCA (middle panel) maps, overlaid on our optical RGB image (as per Fig. 1).

4.1.1 Morphological properties

From Fig. 3, this source exhibits a relatively bright, central, arc-like component with increasingly faint diffuse emission trailing

north towards the cluster centre at 943 MHz. Faint 'wings' of diffuse emission extend to the east and west of the central arc-like component. At 2.1 GHz, only the brighter central component is visible, implying that the wings and trailing emission are likely steep spectrum in nature.

We measure a largest angular size (LAS) of 8.7 arcmin at 943 MHz, which corresponds to a largest linear size (LLS) of 579 kpc. While this is smaller than many relics, this LLS is not unusual. We also highlight that the relic is slightly less extended at 2.1 GHz, where we measure an LAS ∼6 arcmin, or 394 kpc; this slight decrease in size with increasing frequency is also typical for relics.

At first glance, the morphology of this relic appears contradictory – the concave shape appears to imply a merger shock travelling from the south to the north, whereas the brightness distribution visibly declining towards the cluster centre would imply a shock propagating from north to south. As such, this source has been dubbed a 'wrong-way' relic.[7] While radio relics with similar morphologies are uncommon, ours is not the only example: highly sensitive low-frequency observations have begun to reveal other concave relics (HyeongHan et al. 2020; Botteon et al. 2021).

Simulations suggest that highly complex cluster merger events involving multiple subclusters can generate inhomogeneous shock structures that generate concave radio relics similar to that observed here (Skillman et al. 2013, Wittor et al., in preparation). As indicated by Dehghan et al. (2017), Abell 3266 exhibits high velocity dispersion and significant substructure, implying a highly complex merger event, and so we suggest this source is likely a radio relic tracing a shock propagating in a N-S direction following the main cluster merger.

4.1.2 *Spectral properties*

The lower panel of Fig. 3 presents the spectral index map of the 'wrong-way' relic between 943 MHz and 2.1 GHz. From Fig. 3, the median spectral index is $\langle\alpha\rangle = -1.7$. Towards the south, at the presumed leading edge of the relic where particle acceleration is expected to occur due to the shock, the spectral index is marginally flatter with a median of $\langle\alpha\rangle = -1.4$. The spectral index steepens significantly towards the north in the presumed downstream region, reaching values around $\alpha \sim -2$. The typical uncertainty in the spectral index map is about 0.1 to 0.2. This clear spectral gradient is typical of radio relics, as the synchrotron-emitting electrons age in the wake of the passing shock, which is located at the leading edge of the source. We note that the internal spectral indices from MeerKAT indicate steeper spectral indices for the relic than shown in Fig. 3. However, since the robustness of these spectral indices as a function of distance from the pointing centre are still being studied, we adopt the current measurements for the purpose of our discussion.

While the LAS of the relic is around half the theoretical LAS accessible by our ATCA data, to check whether we were missing any flux from our ATCA image due to scale size sensitivity, we repeated this analysis using images produced with matched *uv*-coverage, applying an inner *uv*-cut of 122λ to our ASKAP data. From our *uv*-matched images, we find negligible difference in the measured flux density. As such, we are confident that our following analysis is not biased by inconsistencies in angular scale sensitivity. However, in the downstream region, the faint steep-spectrum emission may be too faint to recover by the ATCA at 2.1 GHz. Much deeper observations would be required to probe the spectral index of the emission in this region.

[7]Priv. comm. Kenda Knowles.

Table 4. Integrated flux density measurements for the 'wrong-way' relic in Abell 3266.

Instrument	Frequency (MHz)	Integrated flux density ASKAP-matched (mJy)	Integrated flux density MWA-matched (mJy)
ASKAP	943	72.3 ± 7.4	77.3 ± 7.8
MeerKAT	1043	72.1 ± 7.4	73.8 ± 7.4
MeerKAT	1092	65.4 ± 6.7	67.8 ± 6.9
MeerKAT	1312	37.2 ± 3.8	39.3 ± 4.0
MeerKAT	1381	33.2 ± 3.4	34.7 ± 3.5
MeerKAT	1448	29.7 ± 3.1	30.3 ± 3.1
MeerKAT	1520	25.1 ± 2.6	28.7 ± 2.9
MeerKAT	1656	17.8 ± 1.8	20.6 ± 2.1
ATCA	2100	10.3 ± 0.6	11.8 ± 0.7

Notes. The 'ASKAP-matched' column reports the measurement integrated over the area defined by the 3σ contour in the top panel of Fig. 3; the 'MWA-matched' column reports the measurement integrated over the full extent of the relic measured in fig. 1 of Duchesne et al. (2022). In all cases, contaminating compact sources have been excised.

Integrating over the area defined by the 3σ contour of 15-arcsec ASKAP map presented in Fig. 3, we measure a total flux density of $S_{943\,\mathrm{MHz}} = 72.3 \pm 7.4$ mJy with ASKAP and $S_{2.1\,\mathrm{GHz}} = 10.3 \pm 0.6$ mJy with the ATCA (after removing compact source contamination). To explore the broad-band SED of the 'wrong-way' relic further, we integrated over the same area in the MeerKAT GCLS subband images selected for this work, as well as including flux density measurements from the MWA and KAT-7 reported by Duchesne et al. (2022). Our new flux density measurements are reported as the 'ASKAP-matched' measurements in Table 4. For consistency, we also integrated over the area of the relic defined in fig. 1 of Duchesne et al. (2022). These larger area measurements are consistent to within 1σ to 2σ; we also report them as the 'MWA-matched' measurements in Table 4. The broad-band integrated SED between 88 MHz and 2.1 GHz, derived using the ASKAP-matched measurements, is presented in Fig. 4.

From Fig. 4, the 'wrong-way' relic exhibits clear departure from a single power-law behaviour, atypical for relics associated with merger shocks. To the best of our knowledge, only two relics in the literature have previously been reported with broken power-law spectra: the relic in Abell 2256 (Owen et al. 2014; Trasatti et al. 2015) and the North Relic in ZwCl 2341.1 + 0000 (Parekh et al. 2022). However, recent work has shown that the relic in Abell 2256 in fact shows single power-law behaviour up to at least 3 GHz (Rajpurohit et al. 2022). Furthermore, the SED for the North Relic in ZwCl 2341.1 + 0000 presented by Parekh et al. (2022) shows measurements at only four frequencies, so while the SED steepens it does not follow a clearly different power law at higher frequencies. With the addition of JVLA data in the 2–4 GHz range originally reported by Benson et al. (2017), both relics in ZwCl 2341.1 + 0000 appear to follow a single power law across the frequency range 610 MHz to 3 GHz.

Our analysis involves broad-band data across a much wider frequency range, with clear – and distinctly different – power-law behaviour at both high and low frequencies. As such, the 'wrong-way' relic in Abell 3266 is arguably the clearest example of a relic that shows significant spectral steepening reported to-date.

To quantify the spectral steepening, we approximate both the low-frequency part ($\nu \leq 943$ MHz) and the high-frequency part

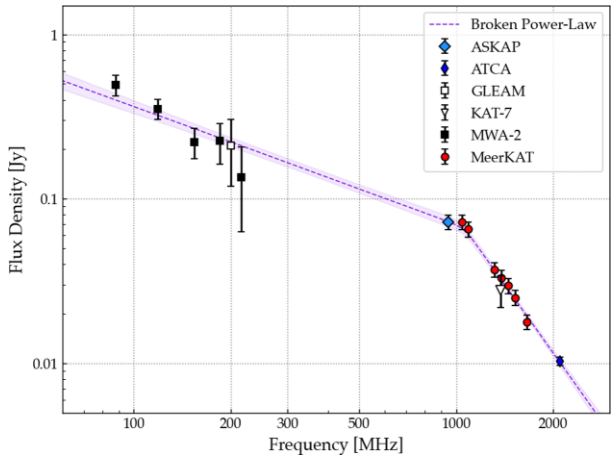

Figure 4. Integrated SED for the 'wrong-way' relic to the SE of Abell 3266 (Source D1; shown in Fig. 3). Our new ASKAP and ATCA integrated flux density measurements are shown as diamonds; our measurements from the public GCLS maps (Knowles et al. 2022) are shown as red circles. We also report flux density measurements from the MWA and KAT-7 (Duchesne et al. 2022). The purple line shows our best-fitting broken power-law spectrum; the shaded region denotes the 1σ uncertainty.

($\nu \geq 943$ MHz) with a power-law spectrum. We used an 'affine invariant' Markov chain Monte Carlo (MCMC) ensemble sampler (Goodman & Weare 2010) as implemented by the EMCEE package (Foreman-Mackey et al. 2013) to constrain the model parameters of this broken power-law fit. The best-fitting SED model, along with the 16th and 84th percentile uncertainty region, is plotted in Fig. 4. Our modelling yields a low-frequency spectral index $\alpha_{\rm low} = -0.72 \pm 0.06$ below the break frequency ($\nu_{\rm b} = 1056 \pm 49$ MHz) and $\alpha_{\rm high} = -2.76 \pm 0.15$ above this frequency. This high-frequency spectral index is extremely steep for radio relics.

Given the spectral index convention we adopt, the k-corrected radio power P_ν at frequency ν is given by the following equation:

$$P_\nu = 4\pi\, D_{\rm L}^2\, S_\nu\, (1+z)^{-(1+\alpha)} \tag{1}$$

where $D_{\rm L} = 255$ Mpc is the luminosity distance at the cluster redshift of $z = 0.0594$, and S_ν is the flux density at frequency ν. Based on our broad-band SED fit presented in Fig. 4, we use equation (1) to derive a radio power of $P_{1.4\,\rm GHz} = (2.38 \pm 0.10) \times 10^{23}$ W Hz^{-1}. While this places the 'wrong-way' relic in Abell 3266 towards the low-power end of the known population, it is not visibly an outlier in typical scaling relation planes between radio relic power and cluster mass, for example (Duchesne et al. 2021a; Duchesne, Johnston-Hollitt & Bartalucci 2021d).

4.1.3 *Acceleration mechanisms*

The commonly accepted theoretical framework for generating radio relics is DSA, whereby a population of electrons are accelerated to the relativistic regime by merger shocks. These shocks are often detectable at X-ray wavelengths, presenting as a jump in the ICM density, pressure, and/or temperature. While our *XMM–Newton* mosaic covers a large area, including deep integrations on both the cluster centre as well as the outskirts, there is insufficient S/N to perform a meaningful investigation into the ICM properties at the location of the 'wrong-way' relic. However, Sanders et al. (2022) report the presence of a shock at a distance of 1.1 Mpc from the cluster centre measured with eROSITA, consistent with the position of the relic. Depending on whether the pressure jump or density jump is used to trace the discontinuity, Sanders et al. find a Mach number $\mathcal{M}_{\rm X\text{-}ray} \sim 1.54$–$1.71$.

Cluster merger shocks in the ICM can be considered as quasi-stationary if the time-scale on which the geometry and/or shock strength changes is much greater than the cooling time-scale of the synchrotron-emitting electrons. Under this stationary shock situation, the integrated spectral index $\alpha_{\rm int}$ is slightly steeper than the injection index $\alpha_{\rm inj}$, following

$$\alpha_{\rm int} = \alpha_{\rm inj} - 0.5. \tag{2}$$

Assuming the underlying physical mechanism responsible for generating the relic is a form of DSA, the relationship between the radio-derived shock Mach number and the injection index takes the following form:

$$\mathcal{M}_{\rm radio} = \left(\frac{2\alpha_{\rm inj} - 3}{2\alpha_{\rm inj} + 1}\right)^{1/2}, \tag{3}$$

originally presented by Blandford & Eichler (1987).

However, as shown in Fig. 4, the integrated spectrum of the 'wrong-way' relic shows significant steepening. Thus, if the 'wrong-way' relic is caused by a shock front that propagates into the cluster outskirts, the shock front may not cause radio emission according to the quasi-stationary shock scenario, and simply determining the Mach number using the *integrated spectral index* is invalid; instead we use the *observed spectral index* at the shock front to represent the injection index in equation (3). To better explore the substructure at the shock front, we profiled our spectral index map using adjacent boxes of 15-arcsec width, spaced across the long axis of the relic. The regions used, along with the resulting spectral index and Mach number profile, are presented in Fig. 5.

From Fig. 5, we find a median spectral index of $\langle\alpha\rangle = -1.48 \pm 0.14$ at the leading edge of the relic. We also see that the spectral index profile of the 'wrong-way' relic varies somewhat across its length, though is typically in the range $-1.75 \lesssim \alpha \lesssim -1.25$ across the majority of regions. Several regions towards the easternmost edge of the relic show significantly varying spectral behaviour. While the S/N is lower at these extremes (and thus the uncertainty is greater), the divergence from the median value is significant, perhaps indicating different physical conditions.

The Mach number profile in the lower right-hand panel of Fig. 5 indicates that the 'wrong-way' relic traces a distribution of weak Mach numbers $1.4 \lesssim \mathcal{M} \lesssim 2.3$, with a median value of $\langle\mathcal{M}\rangle = 1.74 \pm 0.23$. As we are measuring the variations in spectral index locally, we are resolving spectral variations across the leading edge of the relic (and hence variations in the strength of the shock). Simulations by Wittor et al. (2021) for example show that the Mach number distribution generated by cluster mergers is broader, with a typically lower average Mach number, than is inferred from the integrated spectral index (which traces the *radio-weighted Mach number*). Such behaviour is also seen in some other well-studied relics (e.g. Di Gennaro et al. 2018; Rajpurohit et al. 2018, 2021b).

Some previous studies show tension between radio- and X-ray-derived Mach numbers (e.g. Akamatsu et al. 2017; Urdampilleta et al. 2018) and while it may indicate underlying problems with our understanding of the DSA mechanism, recent simulations have gone some way to reconciling the discrepancy. Wittor et al. (2021) showed that the radio emission from relics traces a *distribution* of Mach numbers, and is hence sensitive to high Mach number shocks at the tail of the distribution, whereas the X-ray emission provides a better tracer of the *average* of the Mach number distribution. Additionally, Dominguez-Fernandez et al. (2021) showed that the properties of radio relics are heavily influenced by the properties of the ICM, and

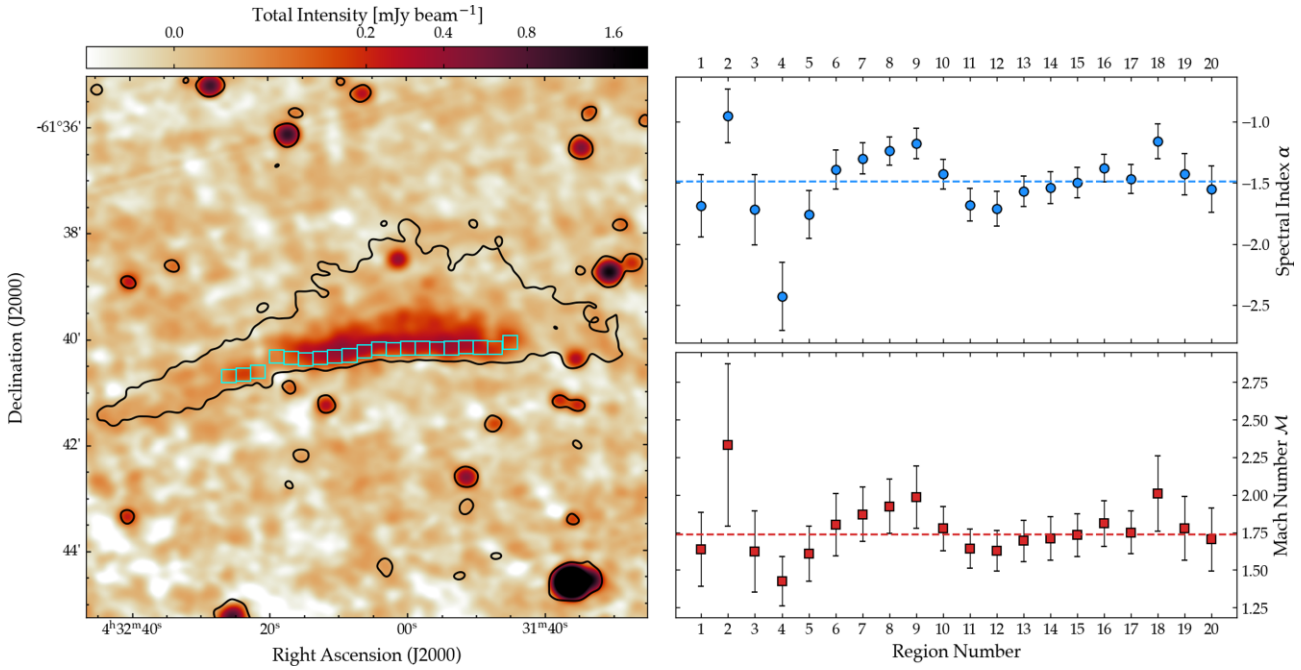

Figure 5. Left-hand panel*:* radio surface brightness maps of the 'wrong-way' relic at 15-arcsec resolution. The colourmap shows our ATCA image at 2.1 GHz; the black contour shows the 4σ contour from our ASKAP map. Cyan boxes show 15-arcsec regions used to profile the spectral index and Mach number. Box numbers increase monotonically from the left- to right-hand side. Right-hand panels*:* profile of the spectral index α (*upper*, in blue) and Mach number $\mathcal{M}$ (lower, in red) for regions shown in the left-hand panel. Dashed lines show the median values of the spectral index, $\langle\alpha\rangle = -1.48 \pm 0.14$, and Mach number, $\langle\mathcal{M}\rangle = 1.74 \pm 0.23$, for the respective subplot.

that fluctuations in the ICM (due to turbulence, for example) also act to reconcile the tension between $\mathcal{M}_{\text{X-ray}}$ and $\mathcal{M}_{\text{radio}}$.

Overall, our radio-derived Mach number would appear to be consistent with the X-ray-derived Mach number. However, we note that given the clear spectral steepening in the SED, the injection index cannot be inferred from this radio Mach number. The low radio Mach number we have derived from the spectral index would result in a relic with an observed luminosity based on the classical DSA scenario for radio relics, which clearly cannot be the case.

4.1.4 On the nature of the 'wrong-way' relic

The 'wrong-way' relic in Abell 3266 is a highly atypical example of its kind. To summarize our findings: (i) its morphology is somewhat unusual, although it is not the only example of a concave relic in the literature (e.g. HyeongHan et al. 2020; Botteon et al. 2021); (ii) it coincides with an X-ray shock that exhibits a low Mach number; (iii) it shows clear spectral steepening in the downstream region; and (iv) it exhibits significant steepening in the integrated spectrum, with a high-frequency spectral index that is extremely steep for a radio relic, and a low-frequency spectral index that is flatter than is expected for an injection-plus-ageing electron population generated by the standard quasi-stationary shock scenario (which would require a spectral index steeper than -1). The clear downstream spectral index trend favours the classification as radio relic and disfavours alternative explanations (such as a radio phoenix). The 'wrong way' morphology is exceptional since it combines evidence for being caused by the shock front with an extreme spectral steepening. It is challenging to find a plausible scenario for the extreme steepening.

One of the big open questions in studies of DSA in radio relics is whether the shock is efficient enough to accelerate electrons from the thermal pool to the relativistic regime, or whether a pre-existing population of mildly relativistic electrons is required. Such a population may have been injected over the course of a cluster's lifetime by radio galaxy jets, for example. The majority of the more powerful radio relics appear to challenge standard DSA from the thermal pool, requiring unphysically large acceleration efficiency to generate the observed high radio luminosity (e.g. Kang & Ryu 2011; Botteon et al. 2016a, 2020b). However, some radio relics appear to be consistent with acceleration directly from the thermal pool (e.g. Botteon et al. 2016b, 2020b; Locatelli et al. 2020).

In the case of the 'wrong-way' relic, the clear spectral steepening seen in the integrated spectrum (Fig. 4) provides strong evidence of a more complex scenario than standard DSA. Alternatives to the standard DSA scenario have been proposed, such as the shock *re*-acceleration of a pre-existing mildly relativistic electron population (e.g. Kang & Ryu 2011, 2016) or an electron population that experiences multiple shocks (Inchingolo et al. 2022). It is of particular interest to note the morphological and spectral similarities between the 'wrong-way' relic in Abell 3266 and 'Relic B' in the simulations of Inchingolo et al. (2022), which also shows a somewhat concave morphology.

However, both of these alternative scenarios generate integrated spectra that are *curved* rather than showing the striking broken power law seen in Fig. 4. To the best of our knowledge, there is currently no physically motivated theoretical framework that can generate this spectrum. This motivates deeper theoretical work to determine the exact physical conditions required to yield broken power-law behaviour seen in Fig. 4. One potential avenue for investigation would be to examine whether alternative scenarios could lead to a significantly curved spectrum at injection. However, such work is beyond the scope of this paper.

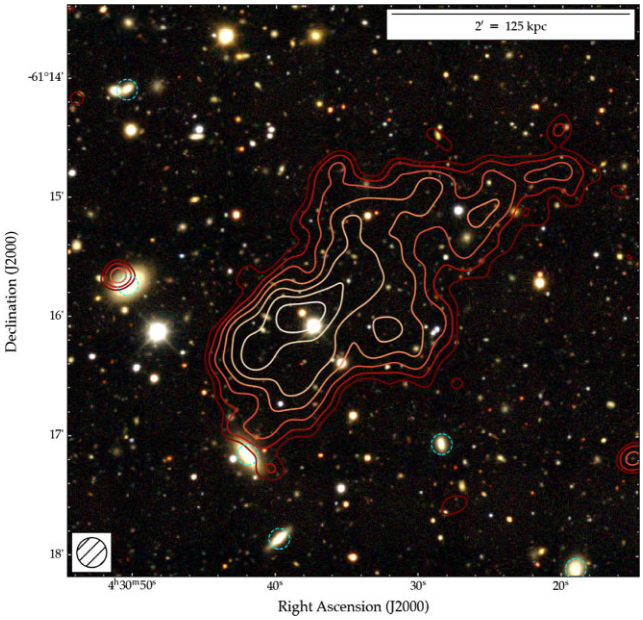

Figure 6. Radio-on-optical overlay of the ultrasteep spectrum fossil radio galaxy to the NW of Abell 3266 (source 'D2' in Fig. 1). Contours show the 943-MHz ASKAP surface brightness at 15-arcsec resolution, starting at 3σ and scaling by a factor of $\sqrt{2}$. The colourmap shows an optical RGB image from DES, as per Fig. 1. Dashed cyan circles denote cluster-member galaxies identified by Dehghan et al. (2017). The proposed host for this diffuse radio source is the cluster-member galaxy at the SE tip of the emission.

4.2 Source D2: an ultrasteep spectrum fossil

This source, first reported by Duchesne et al. (2022), lies to the NW of the cluster centre. It is asymmetric and moderately extended at 943 MHz, with an LAS of 3.6 arcmin. It is undetected by the ATCA at 2.1 GHz. Fig. 6 presents the ASKAP surface brightness contours of this source, overlaid on our RGB image from DES (as per Fig. 1).

Two possible optical counterparts are visible in Fig. 6. One aligns roughly with the radio centroid, but cannot be the host as it is a foreground star, so we suggest that the cluster-member galaxy towards the SE tip of the emission (identified by Dehghan et al. 2017) was the likely original host of this diffuse radio source. The cluster-member galaxy J043041.92−611709.7 has a redshift $z = 0.05587$ and is a member of Structure 5, one of the subgroups surrounding the core of Abell 3266 (see Dehghan et al. 2017). This suggests a projected LLS of 223 kpc.

The diffuse, highly asymmetric nature of this object, combined with the lack of an identifiable core at either 943 MHz or 2.1 GHz, supports the suggestion by Duchesne et al. (2022) that this is a fossil source originally associated with J043041.92−611709.7. Following this scenario, the fossil radio jets extend out from Structure 5 into the region between Structures 3 and 4, where no cluster-member galaxies have been identified. There are a variety of assessment criteria for selecting candidate remnant radio galaxies, including morphological properties, ultrasteep (and curved) spectral index, and core prominence (CP), that have been used in numerous previous remnant studies (Brienza et al. 2017; Mahatma et al. 2018; Jurlin et al. 2021; Quici et al. 2021). The morphological properties are consistent with the proposed remnant scenario; we will now consider the spectral properties and CP.

Table 5. Integrated flux density measurements for source D2, the ultrasteep spectrum fossil to the NW of Abell 3266.

Instrument	Frequency (MHz)	Integrated flux density ASKAP-matched (mJy)	Integrated flux density MWA-matched (mJy)
ASKAP	943	26.9 ± 2.7	27.8 ± 3.0
MeerKAT	1043	12.5 ± 1.3	12.5 ± 1.3
MeerKAT	1092	9.4 ± 1.0	9.5 ± 1.0
MeerKAT	1312	1.9 ± 0.2	2.4 ± 0.3
MeerKAT	1381	1.3 ± 0.2	1.6 ± 0.2

Notes. The 'ASKAP-matched' column reports the measurement integrated over the area defined by the 3σ contour of Fig. 6. The 'MWA-matched' column reports the measurement integrated over the full extent of the fossil measured in fig. 1 of Duchesne et al. (2022), after subtracting compact sources within the region. This source becomes undetectable in the MeerKAT GCLS maps above 1381 MHz due to its ultrasteep spectrum.

4.2.1 *Spectral properties*

ASKAP measures a peak flux density of $S_{\rm pk,\,943\,MHz} = 1.48$ mJy beam^{-1} in our 15-arcsec-resolution image. Despite achieving an rms of 13.9 μJy beam^{-1} with the ATCA, this source remains undetected at 2.1 GHz. As such, taking a conservative 2σ upper limit, we can place an upper limit of $\alpha^{2.1\,\rm GHz}_{943\,\rm MHz} \leq -4.9$ on the spectral index of this object in the frequency range 943 MHz to 2.1 GHz. This is an extremely steep spectrum, approaching the steepest spectral index measured to-date (Hodgson et al. 2021), although the spectral index measured by Hodgson et al. is at much lower frequency, implying an older population of electrons.

At much lower resolution, this ultrasteep-spectrum diffuse object in Abell 3266 has been previously catalogued as part of the GaLactic and Extragalactic All-sky MWA survey (GLEAM; Wayth et al. 2015). The GLEAM Extragalactic Catalogue (Hurley-Walker et al. 2017) object is GLEAM J043032−611544; it is an unresolved source with a 200-MHz flux density of $S_{\rm int,\,200\,MHz} = 1.45 \pm 0.14$ Jy. Despite comparable sensitivity and resolution, it is also undetected by KAT-7, supporting the suggestion of an extremely steep spectral index. Duchesne et al. (2022) present images of this cluster from the Phase II MWA; they find that this source has a steep low-frequency spectral index $\alpha^{216\,\rm MHz}_{88\,\rm MHz} = -1.70 \pm 0.14$. This steep spectral index implies an aged plasma, even at low radio frequencies.

Integrating above the 3σ contour, ASKAP measures an integrated flux density of $S_{\rm int,\,943\,MHz} = 26.8 \pm 2.7$ mJy. We use this measurement in conjunction with the low-frequency Phase II MWA measurements presented by Duchesne et al. (2022), plus measurements made on the MeerKAT GCLS data products, to explore the broadband integrated SED for this fossil source. As for the 'wrong-way' relic, we report two sets of measurements: an 'ASKAP-matched' flux density, integrated over the area defined by the 3σ contour in Fig. 6, and an 'MWA-matched' flux density, integrated over the area defined in fig. 1 of Duchesne et al. (2022). These larger area measurements are also broadly consistent with the ASKAP-matched measurements. Our measurements are listed in Table 5 and the integrated SED for Source D2 (using our 'ASKAP-matched' measurements) is presented in Fig. 7.

It is immediately striking that the SED is highly curved, and the deeper data provided by ASKAP and MeerKAT are consistent with the upper limits from KAT-7 (Riseley 2016; Duchesne et al. 2022). The spectra of remnants are often described using models such as the 'JP' model (Jaffe & Perola 1973), the 'KP' model (Kardashev 1962; Pacholczyk 1970), or a form of the 'continuous injection' or 'CI' model (Komissarov & Gubanov 1994). The 'CI' model describes the

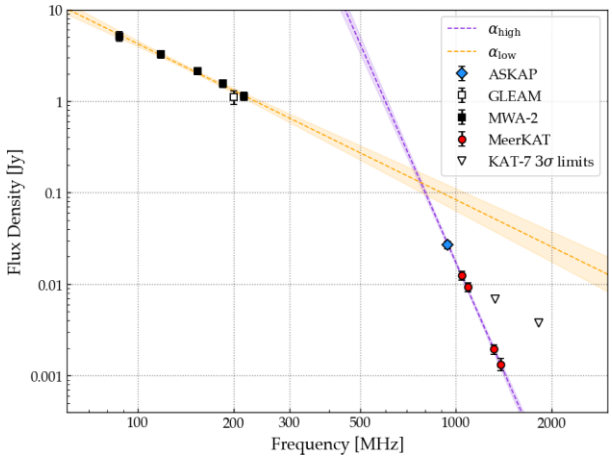

Figure 7. Spectral energy distribution (SED) for the ultrasteep spectrum fossil to the NW of Abell 3266 (Source D2; shown in Fig. 6). Our new ASKAP measurement is shown by the blue diamond; datapoints from the MWA (Duchesne et al. 2022) are shown as squares. Open triangles denote 3σ upper limits from KAT-7. In-band spectral measurements from the MeerKAT GCLS data (where the source was detectable above 3σ) are shown in red. The spectral index is extremely steep, approximated by a power-law fit of $\alpha_{\rm low} = -1.70 \pm 0.14$ between 88 and 216 MHz and $\alpha_{\rm high} = -7.92 \pm 0.30$ between 943 and 1312 MHz. These fits are shown as dashed lines, with the shaded region denoting the 1σ uncertainty.

spectrum arising from an electron population injected over a period from $t = 0$ to τ, where τ is the source age. Two versions of the 'CI' model exist: 'CI-on', where energy injection is still occurring, and 'CI-off', where the injection ceased some period of time ago ($\tau_{\rm off}$). These models all predict a spectrum that becomes increasingly steep and curved as a source ages, with spectral break that moves to increasingly lower frequencies. We attempted to fit 'JP', 'KP', and 'CI-off' models using the SYNCHROFIT package (developed as part of Quici et al. 2022).[8] None provided a good description of the SED behaviour shown in Fig. 7.

This is unsurprising: the ultrasteep low-frequency spectral index $\alpha^{216\ {\rm MHz}}_{88\ {\rm MHz}} = -1.70 \pm 0.14$ measured by Duchesne et al. (2022) implies an injection index that is steeper than is expected from theory, and cannot be replicated by any of the aforementioned models. We approximated the high-frequency spectral index using a power-law fit to the measurements between 943 and 1381 MHz from Table 5, finding a value of $\alpha_{\rm high} = -7.92 \pm 0.30$. This is extremely steep, and is not replicated by any of the physically motivated models. Overall, it is likely that the spectral break for source D2 occurs below the observing band of the MWA, similar to the ultrasteep spectrum 'jellyfish' source reported by Hodgson et al. (2021).

From equation (1), we can estimate the k-corrected 1.4-GHz radio luminosity. We must make some assumptions however; we assume that (i) our identification of the host galaxy is correct ($z = 0.055\,87$; Dehghan et al. 2017) and (ii) the spectral index is reasonably approximated by the ultrasteep power-law fit to our ASKAP and MeerKAT measurements. While the flux density of source D2 drops precipitously at these frequencies, and as such our modelling likely overestimates the 1.4-GHz flux density, we estimate an upper limit to the 1.4-GHz flux density of $S_{1.4\ {\rm GHz}} = 1.35 \pm 0.14$ mJy. Equation (1) yields an upper limit radio luminosity of $P_{1.4\ {\rm GHz}} = (1.36 \pm 0.13) \times 10^{22}$ W Hz^{-1}.

[8]Currently available at https://github.com/synchrofit/synchrofit.

4.2.2 *Core prominence*

The CP quantifies the brightness of the radio core, compared to the total brightness of a radio galaxy. It is defined as the ratio of core flux to total flux, i.e. CP $= S_{\rm core}/S_{\rm int}$. Typically, remnant radio galaxies compiled from historic samples of powerful radio galaxies have a CP $\lesssim 10^{-4}$ (Giovannini et al. 1988); however, more recent, highly sensitive studies suggest that aged remnants may be preferentially deselected if a low CP is used as a criterion (Brienza et al. 2017; Quici et al. 2021).

In the case of our fossil, Source D2, no core is visible at either 943 MHz or 2.1 GHz. We therefore place a conservative upper limit on $S_{\rm core}$ by measuring the local rms noise at the location of the proposed host galaxy, and taking $S_{\rm core,\ 943\ MHz} = 3\sigma_{\rm host} \simeq 0.246$ mJy. The core prominence is therefore CP $\lesssim 10^{-2}$. Thus, this source would not be selected as a remnant *solely* on the basis of CP, consistent with recent statistical studies of AGN remnant populations (Brienza et al. 2017; Quici et al. 2021). Overall, given the radio power derived above, source D2 lies some way below the plane of the CP/$P_{1.4\ {\rm GHz}}$ relation for remnant AGN (e.g. de Ruiter et al. 1990; Jurlin et al. 2021), and is consistent with the USS remnant population modelled by Brienza et al. (2017) for Lockman Hole field, when taking into account both radiative and dynamical evolution.

4.3 Source D3: the central diffuse ridge

We present a zoom on the central region of Abell 3266 in Fig. 8. From our ASKAP map at 15-arcsec resolution, we recover low-level diffuse emission – a diffuse 'ridge' – associated with the central region of Abell 3266. The LAS of this emission is 218 arcsec, corresponding to an LLS of 240 kpc. Integrating above the 3σ contour and excising the contribution from the three largely compact radio galaxies embedded in this diffuse emission (including the BCG), ASKAP recovers a total integrated flux density of $S_{943\ {\rm MHz}} = 7.95 \pm 0.78$ mJy.

This emission is not detected in our ATCA maps at 2.1 GHz, suggesting a steep spectral index; the typical 943-MHz surface brightness is $\sim$ 150–250 μJy beam^{-1} (around 0.8 μJy arcsec^{-2}). From our 15-arcsec-resolution ATCA map, we measure a typical local rms of 13.1 μJy beam^{-1} (around 0.05 μJy arcsec^{-2}); assuming a 2σ upper limit, we estimate a spectral index of $\alpha^{2.1\ {\rm GHz}}_{943\ {\rm MHz}} \lesssim -2.54$. Such an ultrasteep spectral index would be consistent with a highly inefficient acceleration process such as turbulent acceleration.

This emission is recovered at much lower spatial resolution in the MWA Phase II maps presented by Duchesne et al. (2022), although the resolution is too coarse to make a more accurate determination of the spectral index. Similarly, in the MeerKAT GCLS maps of Abell 3266, this emission is only detected at frequencies below around 1100 MHz, which overlaps heavily with our ASKAP coverage. Given the limited dynamic range of the MeerKAT GCLS maps of Abell 3266 at these frequencies, as well as the narrow lever arm in frequency, any spectral index measurement made between ASKAP and MeerKAT would be highly uncertain.

Given that Abell 3266 is a high-mass cluster undergoing a complex merger event, we might expect the presence of a radio halo. However, the MWA Phase II data presented by Duchesne et al. (2022) show no evidence of a giant radio halo. Using a range of injected radio halo profiles (derived using the scaling relations presented in Duchesne et al. 2021c), Duchesne et al. place an upper limit of $P_{1.4\ {\rm GHz}} \lesssim (0.3\text{–}0.8) \times 10^{24}$ W Hz^{-1} on the luminosity of any halo that may be present, but below the detection limit of the Phase II MWA data. This is around a factor five below expectations from the scaling plane between cluster mass and radio halo power.

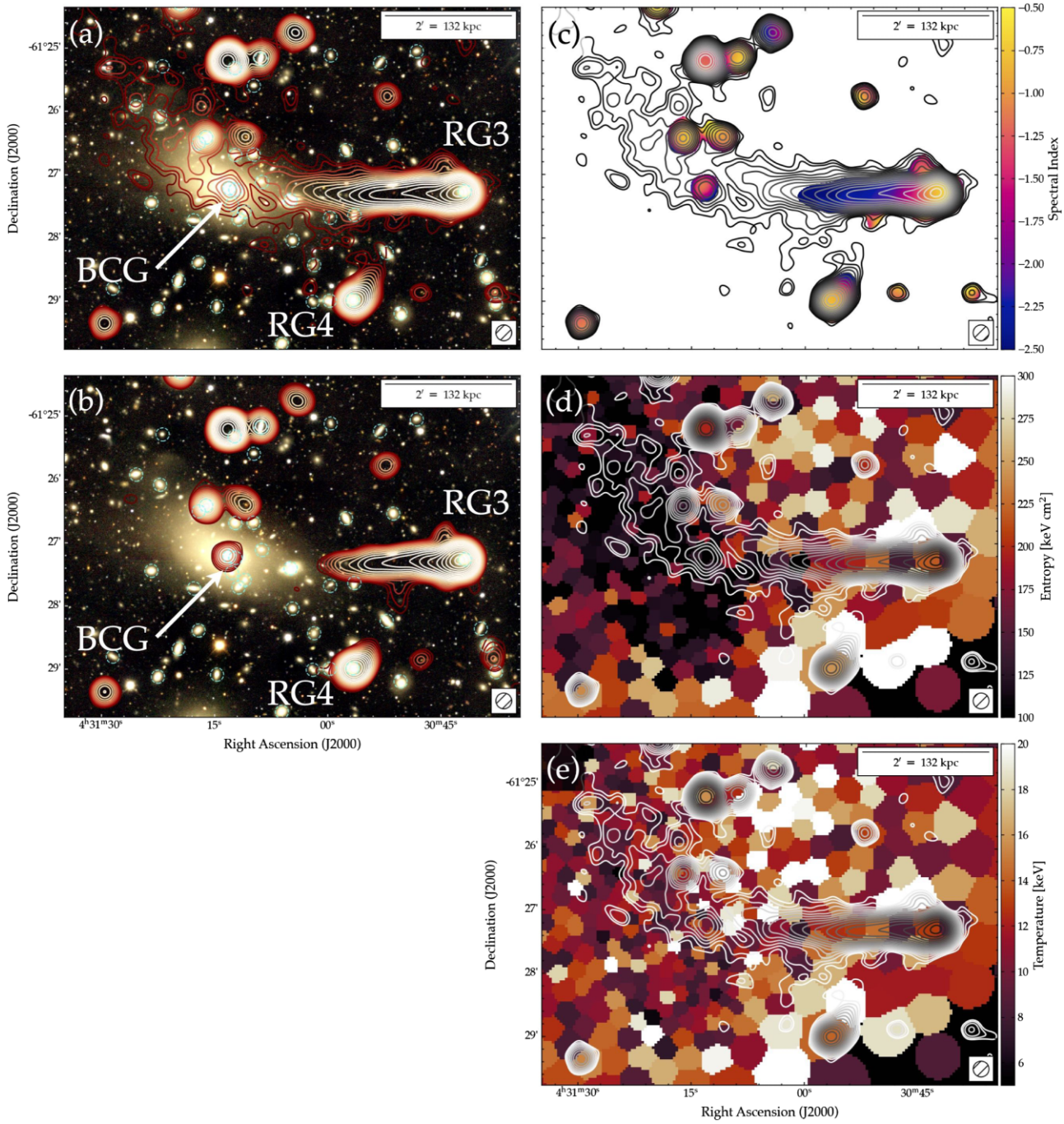

Figure 8. Zoom on the central region of Abell 3266. Panels (a) and (b) show our colour-composite DES image with radio contours from ASKAP at 943 MHz and the ATCA at 2.1 GHz, respectively. Cyan circles identify known cluster-member galaxies. We also highlight two radio galaxies of interest, 'RG3' and 'RG4' as per Fig. 1, as well as the BCG. Panel (c) shows the radio spectral index, derived using our ASKAP and ATCA data. Panels (d) and (e) show the pseudo-entropy and ICM temperature derived from our *XMM–Newton* mosaic. Contours in panels (c)–(e) show the radio surface brightness measured by ASKAP. In all panels, contours are shown at 15 arcsec resolution (indicated by the hatched circle in the lower right-hand corner) and scale by a factor of $\sqrt{2}$ from the 3σ level.

The upper limit to the spectral index implied by our ASKAP and ATCA maps is also far steeper than the typical spectral index of many radio haloes (e.g. Dallacasa et al. 2009; Knowles et al. 2016; Shweta, Athreya & Sekhar 2020; Wilber et al. 2020; Bruno et al. 2021; Duchesne et al. 2021b,d; Rajpurohit et al. 2021a,b). Thus, the nature of this source is not immediately obvious. We explore two potential scenarios for the nature of this source: (i) some form of revived fossil plasma source that originated from one (or more) of the cluster-member radio galaxies, and (ii) a newly detected mini-halo.

4.3.1 Association with cluster-member radio galaxies

In this scenario, the diffuse central ridge could represent fossil plasma from nearby tailed radio galaxies that has been re-accelerated by turbulence in the wake of the cluster merger. Thus, this emission

may constitute some form of 'radio phoenix' (see the review by van Weeren et al. 2019). Radio phoenixes (and other similar revived fossil plasma phenomena) often exhibit an ultrasteep spectrum ($\alpha \lesssim -2$; e.g. de Gasperin et al. 2017; Mandal et al. 2020; Ignesti et al. 2020b), which is consistent with the upper limit to the spectral index derived from our ASKAP and ATCA data.

One obvious candidate for the seed population of this ultrasteep spectrum source is the highly extended head-tail radio galaxy directly west of the emission (source 'RG3'). This galaxy lies at $z = 0.0629$, and is a member of the Western Core Component (WCC; see Dehghan et al. 2017). The WCC is the more massive subcluster in the centre of Abell 3266, it is also relatively compact (compared to the Eastern Core Component) and has high velocity dispersion.

From Fig. 8, the extended tail of this galaxy is about 30 per cent longer at 943 MHz than 2.1 GHz. Much of the faint tail is steep spectrum, with $\alpha_{943\ \mathrm{MHz}}^{2.1\ \mathrm{GHz}} \lesssim -1.5$. The extended tail blends seamlessly into the more extended diffuse central emission. Measured from our ASKAP image at 15-arcsec resolution (top left-hand panel of Fig. 8), the extended tail has a (projected) length of around 205 arcsec, equivalent to 238 kpc. From the lower right-hand panel of Fig. 8, we see that the diffuse central emission is well-bounded by the edge of the low-entropy 'spine' that runs through the cluster centre before deviating sharply to the NE.

An alternative candidate for the origin of the diffuse synchrotron emission is the BCG itself, which lies at the boundary between the two central subclusters (Dehghan et al. 2017). The BCG has a known dumbbell morphology (Henriksen & Tittley 2002; Finoguenov et al. 2006) that is clearly demonstrated in Fig. 8. This morphology, combined with the high relative velocity of the BCG nucleus (327 km s^{-1}; Finoguenov et al. 2006), suggests that the BCG has been tidally disturbed during the cluster merger. We note the presence of extended optical emission in Fig. 8, which broadly follows the morphology of the diffuse radio emission. Thus, the diffuse radio and optical emission may trace the same underlying phenomenon: material that has been disrupted by the close interaction of two galaxies which now constitute the dumbbell BCG and dispersed into the ambient medium.

4.3.2 A mini-halo candidate?

Historically, 'mini-haloes' have typically been found almost exclusively in relaxed, cool-core clusters (Giacintucci et al. 2017; van Weeren et al. 2019). However, next-generation low-frequency observations have blurred the lines significantly, with new detections of multicomponent mini-haloes hosted by moderately disturbed clusters or clusters that show signs of significant core sloshing (Venturi et al. 2017; Kale, Shende & Parekh 2019; Savini et al. 2019; Biava et al. 2021; Knowles et al. 2022; Riseley et al. 2022).

The linear size of source D3, 240 kpc, is typical of known mini-haloes, which are commonly around 100–300 kpc in size (van Weeren et al. 2019), although next-generation observations are revealing that some mini-haloes are significantly larger, up to $\gtrsim 0.5$ Mpc (Savini et al. 2019; Biava et al. 2021; Riseley et al. 2022). Mini-haloes frequently show an association with the radio BCG; from Fig. 8 (panels a and b), we see that several cluster-member radio galaxies, including the BCG, appear embedded in the diffuse emission.

With our measurement of the integrated flux density and our upper-limit spectral index of $\alpha_{943\ \mathrm{MHz}}^{2.1\ \mathrm{GHz}} = -2.54$, we use equation (1) to estimate an upper limit to the total radio power of $P_{1.4\ \mathrm{GHz}} = (2.04 \pm 0.32) \times 10^{22}$ W Hz^{-1}. This extremely low radio power sits almost two orders of magnitude below established scaling relations (Giacintucci et al. 2019; Savini et al. 2019), although another similarly low-power mini-halo candidate ($P_{1.4\ \mathrm{GHz}} \sim 2 \times 10^{22}$ W Hz^{-1}) has recently been reported in the EMU Pilot Survey region by Norris et al. (2021).

It is entirely plausible that the sensitivity to ultra low-surface-brightness emission possessed by ASKAP is allowing us to explore new parameter space in the study of faint diffuse radio sources in clusters of galaxies. However, we note several counterpoints to the mini-halo interpretation. Firstly, our upper-limit spectral index is far steeper than is typically found for mini-haloes ($\alpha \sim -1$; e.g. van Weeren et al. 2019; Biava et al. 2021; Riseley et al. 2022).

Secondly, our *XMM–Newton* temperature map, shown in panel (e) of Fig. 8, does not show strong evidence of a cool core in the region where the diffuse emission is found. Giacintucci et al. (2017) studied the occurrence rates for mini-haloes in a large sample of high-mass ($M \gtrsim 6 \times 10^{14}$ M$_\odot$) galaxy clusters; the occurrence rate is high (~ 80 per cent) for cool-core clusters, and extremely low (~ 0 per cent) for non-cool-core clusters. Only one non-cool-core cluster is known to host a mini-halo: Abell 1413 (Govoni et al. 2009; Savini et al. 2019). At X-ray wavelengths, this cluster exhibits an elongated and slightly disturbed morphology (e.g. Pratt & Arnaud 2002; Botteon, Gastaldello & Brunetti 2018), and exhibits evidence of larger scale diffuse radio emission beyond the known mini-halo (Lusetti et al., in preparation; Riseley et al., in preparation).

Abell 3266 has a high total cluster mass of $M = (6.64^{+0.11}_{-0.12}) \times 10^{14}$ M$_\odot$ (Planck Collaboration XXVII 2016) and shows no evidence of a cool core. As such, the presence of a mini-halo in this system is unlikely, but we cannot conclusively rule out that source D3 is a mini-halo.

4.4 A low-brightness radio halo

Previous searches for a large-scale radio halo in Abell 3266 have been inconclusive, largely due to contamination from discrete sources that could not be excised from lower resolution data (Bernardi et al. 2016; Riseley 2016). Recently, Duchesne et al. (2022) placed the tightest constraints on the presence of a radio halo in Abell 3266, deriving an upper limit of $P_{1.4\ \mathrm{GHz}} \lesssim 0.8 \times 10^{24}$ W Hz^{-1}. Our new data provide the opportunity to perform a deeper search for a faint radio halo.

We applied the multiresolution spatial filtering algorithm introduced by Rudnick (2002b)[9] to our 15-arcsec ASKAP mosaic, using a box size of 48 arcsec. This removes all of the flux from features in the image that are unresolved by our 15-arcsec beam. It removes progressively less of the flux as the scale sizes of the structures increase, reaching a shape-dependent average of ∼50 per cent of the flux on 48-arcsec scales. Since the filter resets the zero level on the map, we corrected the filtered image to an average flux density of zero in extended regions ∼15 arcmin to the NW and to the SE of the cluster centre. We then convolved the filtered image to a resolution of 48 arcsec.

We show this low-resolution image of the central region of Abell 3266 in Fig. 9, along with our *XMM–Newton* X-ray surface brightness mosaic smoothed to the same resolution. Diffuse synchrotron emission fills much of the X-ray emitting volume of Abell 326, which we identify as a radio halo – conclusively detected here for the first time. While much of this emission is associated with the ICM of Abell 3266, we also note residuals associated with the radio galaxies RG2 and RG3. The diffuse emission from the ICM

[9]See also Rudnick (2002a).

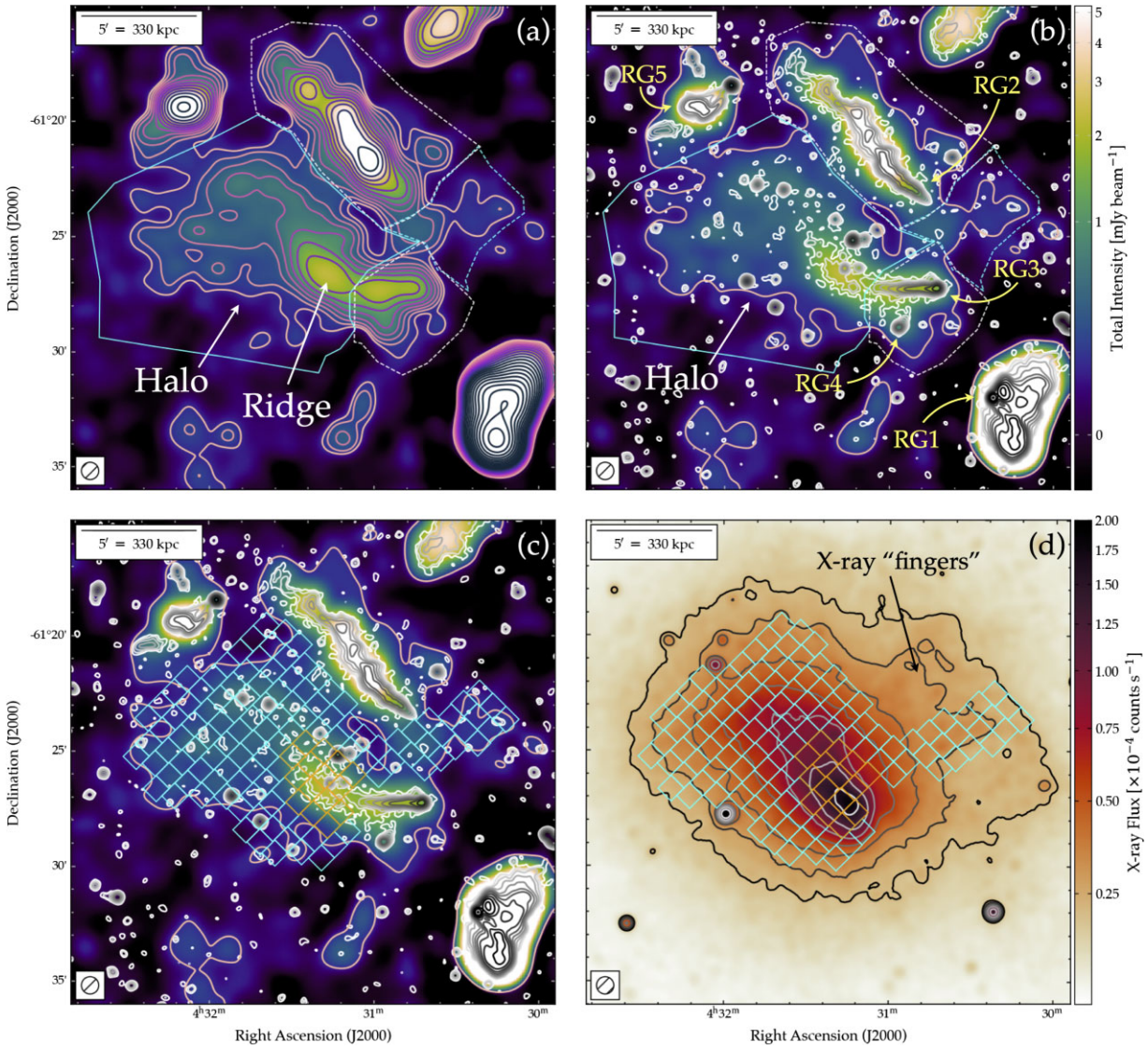

Figure 9. The central region of Abell 3266. Panels (a)–(c) show the our spatially filtered 48-arcsec-resolution ASKAP map at 943 MHz, using the colourbar adjacent to panel (b). Panel (a) shows the low-resolution contours starting at 3σ and scaling by $\sqrt{2}$, where $\sigma = 69.6$ μJy beam^{-1}. Panels (b) and (c) show the 3σ low-resolution contour from panel (a) as well as our 15-arcsec ASKAP contours, starting at 3σ and scaling by factor of 2, for context. Panel (d) shows our *XMM–Newton* mosaic image smoothed with a Gaussian of FWHM 48 arcsec, with representative contours starting at 0.2×10^{-4} counts s^{-1} and scaling by $\sqrt{2}$. Regions in panels (a) and (b) show the area over which the integrated flux density measurements were derived. The boxes in panels (c) and (d) show the regions used to profile the radio/X-ray surface brightness correlation.

fans out to the north, north-east, and east of the narrower band of diffuse emission reported at 15-arcsec resolution.

We also detect a region of diffuse emission associated with the 'fingers' of X-ray emission reported by Henriksen & Tittley (2002), extending to the north-west of the cluster centre. This X-ray surface brightness extension, highlighted in Fig. 9, is also seen in the eROSITA images presented by Sanders et al. (2022); the outer edge of the 'fingers' appears as a sharp discontinuity in the edge-filtered X-ray maps in fig. 8 of Sanders et al. (2022).

To determine the extent of the diffuse emission, we measured east to west across the region defined by the 3σ contour. Including the emission associated with the X-ray 'fingers', the LAS is 16.5 arcmin (1.09 Mpc); conservatively excluding this emission, we measure an LAS of 10.5 arcmin (695 kpc). Both measurements are typical of the scale size of classical radio haloes.

4.4.1 Flux density measurement

The exact coverage of the diffuse radio halo is difficult to determine from the filtered ASKAP map due to confusion from extended components of RG2, RG3, and RG4. We measure the integrated flux density of the radio halo in two ways: (1) obtaining a minimum value assuming the emission region is bounded in the north by RG2 and in the west by RG3/4, and (2) obtaining a maximum value by assuming the diffuse emission extends towards the NW associated with the X-ray 'fingers', and assuming the emission extends into the regions covering by RG2 and RG3/4. To estimate the flux density of the regions containing RG2 and RG3/4, we assume the surface brightness of those regions is equivalent to the mean surface brightness in the adjacent measured regions – the 'fingers' region for RG2 and the central region for RG3/4.

Table 6. Measured properties (largest linear size and integrated flux density) of the diffuse radio halo.

Value	Size (kpc)	$S_{943\ \mathrm{MHz}}$ (mJy)	$S^{\alpha=-1.4}_{216\ \mathrm{MHz}}$ (mJy)	$S^{\alpha=-1.2}_{216\ \mathrm{MHz}}$ (mJy)
Minimum	695	42.2 ± 4.3	330 ± 30	250 ± 30
Maximum	1090	67.8 ± 6.2	530 ± 50	400 ± 40

Note. Here we quote only the statistical uncertainty; see the text for a discussion of systematic uncertainty.

The region over which measurement (1) (the 'minimum' value) was derived is shown by the solid cyan polygon in panel (a) of Fig. 9. Measurement (2) (the 'maximum' value) also incorporates the dashed cyan polygon as well as the halo surface brightness as extrapolated across the dashed white polygons. Integrating above the 3σ contour for these regions we obtain $S^{\mathrm{min}}_{943\ \mathrm{MHz}} = 42.2 \pm 4.3\ (\pm 10.6)$ and $S^{\mathrm{max}}_{943\ \mathrm{MHz}} = 67.8 \pm 6.2\ (\pm 17.0)$ mJy.

When reporting the measurements, we quote two uncertainties: (i) standard statistical uncertainty and (ii) systematic uncertainty. This latter quantity is the dominant contributor to the error budget, and it arises from the uncertainty in determining the correct zero level, which comes from both the possibility of true faint emission very far from the cluster centre, and low-level background variations in the map. We estimate the uncertainty in the zero level to be $\sim$0.1, resulting in a 25 per cent uncertainty in the total flux.

Taking a typical radio halo spectral index of $\alpha = -1.4$ (Duchesne et al. 2021b), these 943-MHz measurements correspond to flux densities at 216 MHz of $330 \pm 30\ (\pm 80)$ and $530 \pm 50\ (\pm 130)$ mJy, consistent with limits reported by Duchesne et al. (2022) for a radio halo of radius 500 kpc at the cluster centre. The larger, second set of uncertainties come from possible errors in the zero level. Measured and extrapolated flux densities are reported in Table 6.

Similarly, we substitute these minimum and maximum values, and the assumed spectral index $\alpha = -1.4$ in equation (1) to derive the minimum and maximum k-corrected 1.4-GHz luminosity. We find values of $P^{\mathrm{min}}_{1.4\ \mathrm{GHz}} = 1.94 \pm 0.20(\pm 0.49) \times 10^{23}$ and $P^{\mathrm{max}}_{1.4\ \mathrm{GHz}} = 3.11 \pm 0.29(\pm 0.78) \times 10^{23}$ W Hz^{-1}.

Comparing these radio luminosity values against established scaling relations, we find that our measurements place the radio halo in Abell 3266 a factor of 4.4–7.1 below the correlation plane for the $P_{1.4\ \mathrm{GHz}}/M_{500}$ relation derived by Duchesne et al. (2021b), consistent with the upper limits from Duchesne et al. (2022).

4.4.2 *Point-to-point correlation: the thermal/non-thermal connection*

As seen in Fig. 9, the extent of the diffuse radio halo matches the extent of the ICM plasma (traced by the X-ray emission), implying a connection between the thermal and non-thermal components. Examining this connection via the correlation between radio surface brightness (I_{R}) and X-ray surface brightness (I_{X}), for example, can provide insights into the particle acceleration mechanism at work (Govoni et al. 2001a). This correlation takes the form $\log(I_{\mathrm{R}}) \propto b \log(I_{\mathrm{X}})$, where b quantifies the slope. Physically, this slope relates to the relative distribution of non-thermal and thermal components, with a superlinear slope (i.e. $b > 1$) indicating that the magnetic field and/or CRe distribution is more peaked than the thermal plasma distribution, whereas a sublinear slope (i.e. $b < 1$) indicates the converse.

We profiled the $I_{\mathrm{R}}/I_{\mathrm{X}}$ connection by placing adjacent boxes of 48-arcsec width across the extent of the 'radio halo'; these regions are also shown in Fig. 9. We excluded any regions that clearly showed association with resolved radio galaxies in our 15-arcsec ASKAP map, to try to mitigate contamination from these sources. Fig. 10 presents our point-to-point correlation, which appears to show a reasonably strong positive trend. To quantify the correlation, we fitted a linear relation (in log-log space) of the form:

$$\log(I_{\mathrm{R}}) = a + b\log(I_{\mathrm{X}}), \tag{4}$$

To determine the optimal values of a and b, we used the MCMC implementation of LINMIX[10] (Kelly 2007). This software package performs Bayesian linear regression, accounting for uncertainties on both variables, intrinsic scatter, and upper limits to the dependent variable (in this case, I_{R}). We take our 'best-fit' values of a and b to be the median values of our MCMC chain, and use the 16th and 84th percentiles to determine the uncertainties. The correlation strength was quantified by measuring the Spearman and Pearson rank coefficients.

Fitting a single population to all our data, we find that the $I_{\mathrm{R}}/I_{\mathrm{X}}$ plane is described by a linear slope of $b_{\mathrm{all}} = 0.99^{+0.07}_{-0.07}$; this slope is shown by the dashed green line in Fig. 10, with the shaded region denoting the uncertainty. Overall, the data are strongly correlated, as we find Spearman (Pearson) coefficients of $r_{\mathrm{S}} = 0.71$ ($r_{\mathrm{P}} = 0.76$). However, a number of regions towards higher X-ray surface brightness show clear departure from a single relation; as such, we also searched for substructure by subdividing our data. We performed our LINMIX regression on the 'ridge' – the emission coincident with source D3 detected at 15 arcsec (orange regions) – and the larger scale 'halo' – those regions that only appear at lower resolution after applying the spatial filter (cyan regions) – separately.

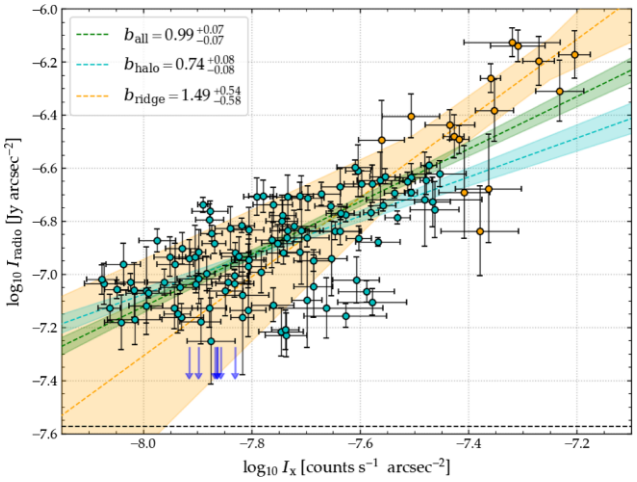

Figure 10. Radio/X-ray surface brightness correlation plane for the 'radio halo' in Abell 3266. We report the radio surface brightness (I_{R}) measured from our spatially filtered 943-MHz ASKAP map at 48-arcsec resolution, and the X-ray surface brightness (I_{X}) measured from our *XMM–Newton* mosaic smoothed with a Gaussian of 48-arcsec FWHM. Markers are coloured according to extraction region (as per Fig. 9). Upper limits (2σ) are shown by blue arrows. Dashed lines and shaded regions correspond to the best-fitting trends from LINMIX, with the slopes shown in the legend, coloured according to the population; the green line denotes the fit performed on *all* regions together. The dashed horizontal line denotes the 1σ level from Fig. 9. Error bars reflect the statistical errors on the measurements.

[10] LINMIX is available through https://linmix.readthedocs.io/en/latest/src/linmix.html.

We found that the 'ridge' regions are described by a superlinear slope of $b_{\rm ridge} = 1.49^{+0.55}_{-0.58}$, whereas the 'halo' regions are described by a sublinear slope of $b_{\rm halo} = 0.72^{+0.09}_{-0.08}$. Each of these subsets shows a strong/moderate-to-strong correlation: for the 'halo', $r_{\rm S} = r_{\rm P} = 0.61$, and for the 'ridge', $r_{\rm S} = 0.66$ and $r_{\rm P} = 0.50$. While the uncertainty on $b_{\rm ridge}$ is significant, and thus the slope is not inconsistent with a linear trend, the values of $b_{\rm ridge}$ and $b_{\rm halo}$ are significantly different. As such, these boxes may trace regions that have a different connection between the thermal and non-thermal components of the ICM.

4.4.3 On the nature of the radio halo in Abell 3266

In general, classical radio haloes have been found to observe *sublinear* scaling relation, i.e. $b < 1$ (Govoni et al. 2001a,b; Giacintucci et al. 2005; Hoang et al. 2019, 2021; Botteon et al. 2020c; Duchesne et al. 2021b; Rajpurohit et al. 2021a,b), whereas mini-haloes have typically been found to follow a *superlinear* scaling relation, i.e. $b > 1$ (Govoni et al. 2009; Ignesti et al. 2020a, 2022; Biava et al. 2021; Riseley et al. 2022). However, there are contrary cases: Timmerman et al. (2021) reported that the mini-halo in the Perseus cluster shows sublinear scaling, whereas de Gasperin et al. (2022) reported that the classical halo in Abell 3667 shows superlinear scaling in the radio/X-ray point-to-point correlation.

The linear slope of $b = 0.99^{+0.07}_{-0.07}$ from our single-population analysis is consistent with the typical $I_{\rm R}/I_{\rm X}$ plane behaviour for radio haloes. However, our two-population analysis shows tentative evidence of substructure: the smaller scale emission traced by the orange regions follows a superlinear trend, typical of mini-haloes, whereas the larger scale emission traced by the cyan regions follows a clearly sublinear trend, typical of haloes.

Multicomponent radio haloes are uncommon but not unprecedented in the literature. The complex merging cluster Abell 2744 also hosts a multicomponent radio halo, where the different components follow distinctly different trends in the $I_{\rm R}/I_{\rm X}$ (Rajpurohit et al. 2021b). Another example is the cluster Abell 2142, which is dynamically disturbed due to merger activity but still hosts a cool core (Wang & Markevitch 2018). Abell 2142 also hosts a multicomponent radio halo, which has alternatively been classified as a 'mini-halo-plus-halo' structure (Venturi et al. 2017). Several other clusters have recently been detected that host both a mini-halo and larger scale diffuse radio emission on scales up to $\gtrsim 0.5$ Mpc (Savini et al. 2018, 2019; Raja et al. 2020; Biava et al. 2021; Riseley et al. 2022, in preparation; Lusetti et al., in preparation). Some of these are known cool-core clusters, some host no clear cool core; all exhibit some level of large-scale disturbance that could inject large-scale turbulence either via core sloshing or minor merger activity.

For example, the cool-core cluster RX J1720.1 + 2638 hosts both a mini-halo and larger scale diffuse emission underlying much of the cluster volume (Biava et al. 2021). In this system, the mini-halo exhibits a clearly *super*linear correlation in the $I_{\rm R}/I_{\rm X}$ plane, whereas the larger scale diffuse emission exhibits a demonstrably *sub*linear correlation; see Biava et al. (2021) for details. This behaviour is consistent with the evidence seen in Fig. 10.

Overall, our findings for Abell 3266 are consistent with the interpretation that we are viewing multicomponent radio halo, although the nature of the smaller scale component remains unclear at present. Given the highly complex merger event occurring in Abell 3266, further work is highly motivated: deeper observations are required to explore the point-to-point correlation in more detail, whereas deeper theoretical exploration of the effect of complex merger events on cluster-scale turbulence and the thermal/non-thermal connection would be required to aid in interpreting our results.

5 RESOLVED RADIO GALAXIES

Abell 3266 hosts a number of other spectacular bent-tail radio galaxies, which are resolved in exquisite detail in our new ASKAP and ATCA maps. These will be discussed in the following subsections.

5.1 RG1: the wide-angle tail radio galaxy

Source RG1 is perhaps the most spectacular radio galaxy hosted by Abell 3266. It is a wide-angle tail radio galaxy, identified variously in the literature as MRC 0429−616 or PKS 0429−61, for example, hosted by the galaxy J043022.01−613200.2 at redshift $z = 0.0557$ (Dehghan et al. 2017). From the optical substructure analysis presented by Dehghan et al., this galaxy is a member of the WCC and lies towards the outermost edge of this subcluster. We present our images of this source at 9-arcsec resolution in Fig. 11.

5.1.1 Radio continuum morphology

RG1 has a compact, bright radio core with jets that point NW and SW with a projected opening angle of around 95°. The NW jet terminates some 20 arcsec (21 kpc) beyond the core, expanding into a relatively bright clump of diffuse radio emission that fades into the larger scale western lobe. Conversely, the SW jet extends much further, with two possible hotspots around 38 arcsec (39.5 kpc) and 77 arcsec (80 kpc) from the core. The outer hotspot marks roughly where the jet expands into the more diffuse southern lobe.

Our high-resolution radio maps presented in Fig. 11 clearly demonstrate that this cluster-member galaxy has undergone a dynamic history and/or experienced complex interactions with the cluster environment. The radio morphology of the lobes is complex: the southern lobe extends to the SW before bending clockwise and sweeping back upon itself, whereas the western lobe extends in an SW direction before turning to the NW. We also note a clear 'hook'-like feature towards the outer edge of the western lobe that is detected by both ASKAP and the ATCA. Finally, we do not clearly detect the western fossil detected by Duchesne et al. (2022) beyond the westernmost edge of the western lobe. This feature is barely visible by-eye in the ASKAP image at 15 arcsec (Fig. 2) but it is not significant compared to the local noise. The non-detection in our ASKAP and ATCA maps is consistent with the ultrasteep spectrum measured by Duchesne et al. for this fossil source ($\alpha = -2.4 \pm 0.4$).

5.1.2 Spectral index distribution

The right-hand panel of Fig. 11 presents the spectral index map of RG1 between 943 MHz and 2.1 GHz. Due to the high S/N achieved by both our ATCA and ASKAP maps, the uncertainty in the spectral index map for RG1 is highly uniform, with values between 0.08 and 0.09; as such, we do not present a map of the spectral index uncertainty.

From the spectral index profile, the core shows a very flat spectrum ($\alpha^{2.1\ \rm GHz}_{943\ \rm MHz} = -0.33$); the jets exhibit fairly typical synchrotron spectra, with $\alpha^{2.1\ \rm GHz}_{943\ \rm MHz} = -0.6$ to -0.8. The jet that feeds the southern lobe shows variations along its length, with flatter-spectrum regions ($\alpha^{2.1\ \rm GHz}_{943\ \rm MHz} \simeq -0.85$) that align well with the hotspots in total intensity and steeper-spectrum regions ($\alpha^{2.1\ \rm GHz}_{943\ \rm MHz} \sim -0.95$) between the hotspots. This behaviour is typical of active jets. The southern

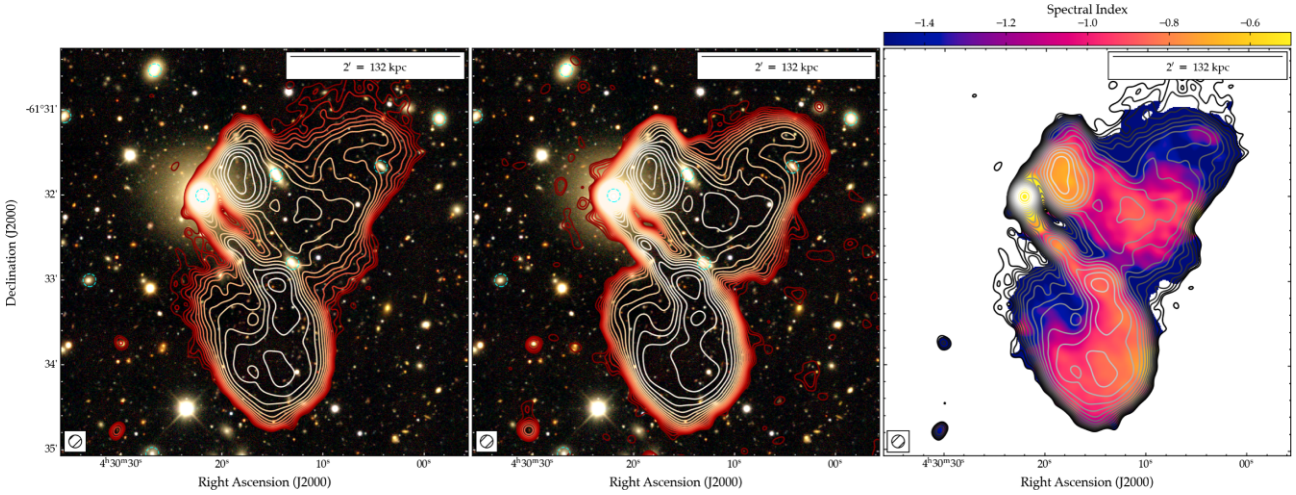

Figure 11. Images of the wide-angle tail radio galaxy to the SE of Abell 3266 (source 'RG1' in Fig. 1) at a resolution of 9 arcsec. The left-hand and centre panels show our RGB image constructed from DES, with 943-MHz ASKAP and 2.1-GHz ATCA contours overlaid, respectively. The right-hand panel shows the radio spectral index, with ASKAP contours overlaid. All contours start at 4σ and scale by a factor of $\sqrt{2}$. Known cluster-member galaxies are identified by dashed cyan circles.

lobe shows a spectral index gradient that broadly follows the surface brightness gradient (with some fluctuations visible).

For the western lobe, the bright 'clump' (where the NW jet presumably terminates) shows a typical synchrotron spectral index $\alpha^{2.1\ \mathrm{GHz}}_{943\ \mathrm{MHz}} = -0.65$ to -0.85, similar to the southern jet. Beyond the 'clump', the spectral index gradient broadly follows the radio surface brightness gradient: The spectral index varies from around $\alpha^{2.1\ \mathrm{GHz}}_{943\ \mathrm{MHz}} \sim -0.85$ at the edge of the clump to $-1.4 \lesssim \alpha^{2.1\ \mathrm{GHz}}_{943\ \mathrm{MHz}} \lesssim -1.0$ towards the edge of the lobe. The 'hook' feature identified in the radio surface brightness also shows a flatter spectral index of $\alpha^{2.1\ \mathrm{GHz}}_{943\ \mathrm{MHz}} \sim -1.3$ compared to the lower surface brightness regions at the extremity of the southern lobe, which show an ultrasteep spectral index (typically $\alpha^{2.1\ \mathrm{GHz}}_{943\ \mathrm{MHz}} \simeq -1.5$ to -2).

Comparing our spectral index map with the MeerKAT in-band spectral index map presented in fig. 1(B) of Knowles et al. (2022), we observe similar spectral behaviour on the whole. However, we also note a number of differences. These are primarily visible in the centroid of the southern lobe, where we measure a typical spectral index of $\alpha^{2.1\ \mathrm{GHz}}_{943\ \mathrm{MHz}} = -0.88$ (at 9-arcsec resolution) whereas the in-band MeerKAT spectral index reaches values as steep as $\alpha^{1.67\ \mathrm{GHz}}_{0.9\ \mathrm{GHz}} = -2.02$ (at 7.1×6.7 arcsec^2 resolution). Similar differences are seen at the outer edge of the bright 'clump' in the western lobe. This discrepancy is too significant to be attributable to measurement uncertainties alone. Given our use of DDFACET's SSD algorithm, which jointly deconvolves emission on a variety of scales and therefore likely recovers the complex spatial distribution of the extended emission from this radio galaxy to a better degree, we suggest that the behaviour seen in the MeerKAT in-band spectral index map is unphysical, and our spectral index map provides a more accurate description of the underlying profile.

5.1.3 On the nature of RG1

Our high-resolution images of RG1 have provided unprecedented detail into the morphology and spectral properties of this active radio galaxy. However, they also raise several questions. What is the nature of the bright 'clump' in the western lobe, and does it correspond to the termination point of the NW jet where it decelerates and expands into the western lobe? What is the dynamical history of this radio galaxy?

Dehghan (2014) attempted to understand the nature of RG1, suggesting that the overall motion of the host galaxy reversed some ∼80 Myr ago. However, numerical simulations of AGN in complex merging clusters would be required to understand more from the theoretical perspective. In order to explore the evolutionary history of this source in detail, we would require additional data at both higher and lower frequencies that is capable of achieving ∼10-arcsec resolution or better. MeerKAT observations with the *UHF*- or *S*-band receiver systems, and/or higher frequency data from the ATCA 4cm band would be suitable, but lower frequency data at sufficient resolution will not be available until the advent of SKA-Low.

5.2 RG2: a complex radio galaxy

Source RG2 lies to the NW of the cluster centre. This source was first identified in relatively shallow narrow-band observations (Murphy 1999; Reid 1999; Murphy & Hunstead 2002). However, the nature of this source has historically remained unclear due to the poor sensitivity and resolution of previous observations. It has previously been hypothesized that this source represents a dying radio galaxy tail, possibly associated with the elliptical galaxy to the immediate SW (Murphy 1999) or alternatively a radio relic (Dehghan 2014). Most recently, Rudnick et al. (2021) present a detailed study of this source (dubbed '*MysTail*' by Rudnick et al.) using data from the MeerKAT GCLS (Knowles et al. 2022). The MeerKAT images presented by Rudnick et al. (2021) and Knowles et al. (2022) clearly demonstrate that this source is a radio galaxy – albeit one that exhibits a highly complex morphology – or may, in fact, comprise multiple radio galaxies. Fig. 12 presents a zoom on our ATCA map of this source at 9-arcsec resolution, with the main features of interest highlighted for reference. We also present ASKAP and ATCA maps of this source at both 9- and 15-arcsec resolution, along with the spectral index map, in Fig. 13.

In our 9-arcsec-resolution ATCA map, we detect a compact radio counterpart to the cluster-member galaxy J043045.37−612335.8 ($z = 0.0628$; Dehghan et al. 2017), at the south-west tip of this source. This is the candidate optical host originally proposed by Murphy (1999), although Dehghan et al. provide the first spectroscopic redshift for this source. The compact radio source is extremely faint,

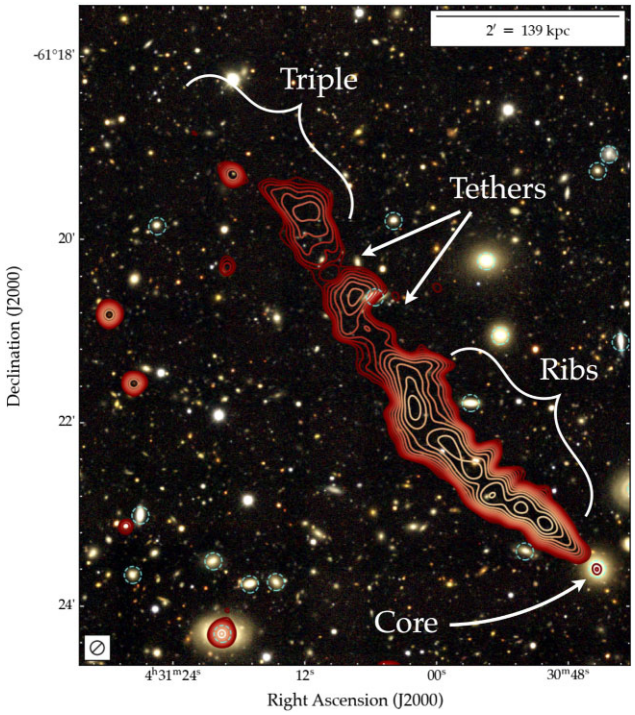

Figure 12. Image of source 'RG2', the complex radio galaxy to the NW of Abell 3266 (dubbed *'MysTail'* by Rudnick et al. 2021), likely associated with the galaxy J043045.37−612335.8 at $z = 0.0628$ (Dehghan et al. 2017). The colourmap shows our RGB image constructed from DES, with cluster-member galaxies highlighted by dashed cyan circles. Contours show the radio surface brightness measured by the ATCA at 2.1-GHz and 9-arcsec resolution, starting at 4σ and scaling by a factor of $\sqrt{2}$. Labels identify key features that are referred to in the text. The north-eastern component of the triple is undetected by the ATCA, suggesting a highly steep spectral index.

with an (unresolved) flux density of $S_{2.1\ \mathrm{GHz}} = 90 \pm 21$ μJy, and it is undetected in our 9-arcsec-resolution ASKAP image, suggesting a flat or inverted spectral index.

Knowles et al. (2022) report a peak flux density measurement of around 65 μJy beam^{-1} in the full-resolution (∼8 arcsec) MeerKAT GCLS image of Abell 3266. Taking this to be the flux density of the (unresolved) radio core, this implies an inverted spectral index around $\alpha^{2.1\ \mathrm{GHz}}_{1.28\ \mathrm{GHz}} \sim +0.7$. We detect no significant emission corresponding to jets from this proposed radio core that feed into the larger scale ribbed tail seen in the images presented here as well as those presented by Rudnick et al. and Knowles et al..

5.2.1 *Integrated spectrum and radio luminosity*

To measure the total integrated flux of RG2, we defined a region corresponding to the 4σ contour of our ASKAP map at 15-arcsec resolution. Integrating over this area, we measure a total flux of $S_{\mathrm{int,\ 943\ MHz}} = 235 \pm 24$ mJy with ASKAP and $S_{\mathrm{int,\ 2.1\ GHz}} = 55 \pm 3$ mJy with the ATCA. This implies an integrated spectral index $\alpha^{2.1\ \mathrm{GHz}}_{943\ \mathrm{MHz}} = -1.81 \pm 0.14$. We combine our new measurements with the lower frequency data presented by Duchesne et al. (2022) and measurements made on the public GCLS images, to investigate the broad-band integrated spectral index of RG2; this is presented in Fig. 14. Overall, the SED exhibits evidence of departure from a single power-law behaviour, so we attempted to model the behaviour with SYNCHROFIT using physically motivated models. We modelled the behaviour using the 'CI-on' and 'CI-off' models, which would represent a radio galaxy observed in an active or remnant phase, respectively. Neither model provided a good description of our data, so we instead defer to a simple broken power-law fit.

This broken power-law fit is also presented in Fig. 14. Our modelling yields a low-frequency spectral index of $\alpha_{\mathrm{low}} = -1.01^{+0.13}_{-0.07}$ below the break frequency and $\alpha_{\mathrm{high}} = -1.67^{+0.13}_{-0.12}$. The break frequency itself is $\nu_{\mathrm{c}} = 0.77^{+0.16}_{-0.17}$ GHz. While the break frequency is relatively poorly constrained, and would require observations with the MeerKAT *UHF*-band receiver system to constrain more accurately, α_{low} and α_{high} are inconsistent, suggesting that the observed spectral steepening is real. Given our cosmology, we use equation (1) and our best-fitting model to derive the radio power, yielding $P_{1.4\ \mathrm{GHz}} = (8.05 \pm 0.02) \times 10^{23}$ W Hz^{-1}.

5.2.2 *Core prominence*

We investigated the CP for RG2, to determine whether it is typical of active or remnant radio galaxies. Using our 2.1-GHz measurements of the integrated flux density and the core flux density, we derive a value of $\mathrm{CP}_{2.1\ \mathrm{GHz}} = 1.6 \times 10^{-3}$. This is entirely consistent with known samples of remnant radio galaxies (Jurlin et al. 2021; Quici et al. 2021). Given the lack of clear jets at 2.1 GHz, as well as the inverted spectral index for the core and the spectral steepening observed in the SED, the question arises: could this represent a phase of restarted AGN activity?

5.2.3 *The ribs and tethers*

From our 9-arcsec-resolution images presented in Figs 12 and 13, we confirm the 'ribbed tail' morphology reported by Knowles et al. (2022, their fig. 19). At this resolution, we find that the 'ribs' are uniformly around 20–30 arcsec wide at half-intensity at both 943 MHz and 2.1 GHz, similar to the width seen by MeerKAT (Rudnick et al. 2021; Knowles et al. 2022).

Examination of the spectral index map presented in the top right-hand panel of Fig. 13 reveals substructure in the spectral index profile of the ribbed tail. There is an overall gradient following the 'spine' of the tail from around $\alpha^{2.1\ \mathrm{GHz}}_{943\ \mathrm{MHz}} \simeq -0.8$ nearest to the proposed optical host to $\alpha^{2.1\ \mathrm{GHz}}_{943\ \mathrm{MHz}} \simeq -1.8$ at the north-eastern end where the ribbed tail fades into the region of the 'tethers'. This is slightly steeper than the the behaviour reported by Rudnick et al. (2021), who measure a spectral index of $\alpha^{1.67\ \mathrm{GHz}}_{0.9\ \mathrm{GHz}} = -0.6$ near the core and $\alpha^{1.67\ \mathrm{GHz}}_{0.9\ \mathrm{GHz}} \sim -1.4$ where the tail bends.

The 'tethers' reported by Rudnick et al. (2021) and Knowles et al. (2022) are also recovered by both ASKAP and the ATCA at 9-arcsec resolution. At 15-arcsec resolution, these blend into each other and form a more contiguous bridge between the brighter knots of the extended RG2 tail. Where the surface brightness is recovered at sufficient S/N, we measure an ultrasteep spectral index of $\alpha^{2.1\ \mathrm{GHz}}_{943\ \mathrm{MHz}} \sim -2.0 \pm 0.2$ for the brighter 'fingers' of emission with an even steeper spectral index of $\alpha^{2.1\ \mathrm{GHz}}_{943\ \mathrm{MHz}} \lesssim -2.5$. Again, our measurements are consistent with the in-band measurements of $\alpha^{1.67\ \mathrm{GHz}}_{0.9\ \mathrm{GHz}} \sim -2$ to -3.4 reported by Rudnick et al.

5.2.4 *The triple*

One of the open questions posed by Rudnick et al. (2021) and Knowles et al. (2022) regards the nature of the 'triple' at the north-eastern end of RG2. Two scenarios exist: the simplest is that the

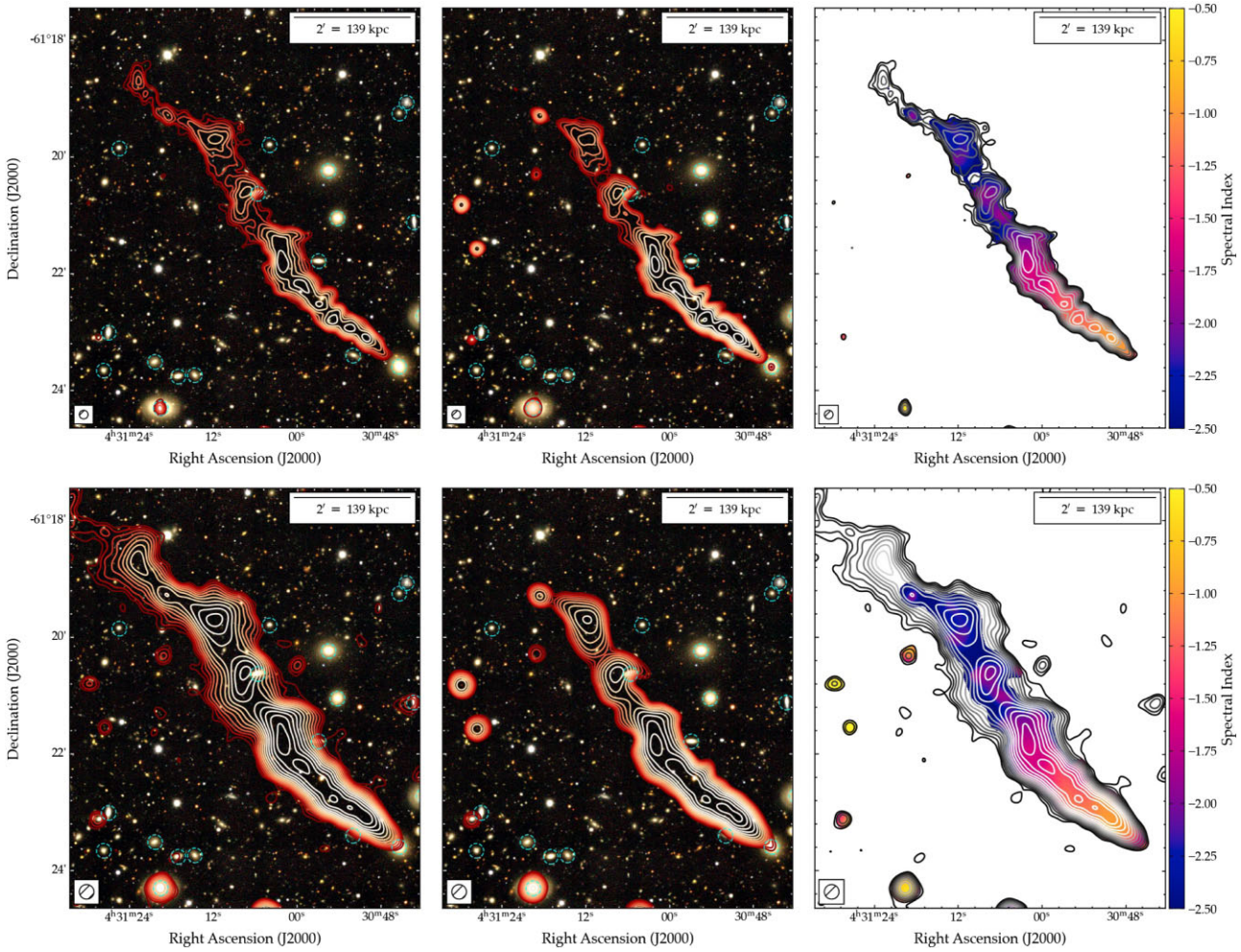

Figure 13. Images of the complex radio galaxy to the NW of Abell 3266 (source 'RG2' in Fig. 1). The top row shows images at 9-arcsec resolution, and the bottom row shows images at 15-arcsec resolution. The left-hand and centre panels show RGB images from DES with 943-MHz ASKAP and 2.1-GHz ATCA contours overlaid, respectively.The right-hand panel shows the radio spectral index, with ASKAP contours overlaid. All contours start at 4σ and scale by a factor of $\sqrt{2}$.

diffuse emission of the 'triple' is simply a continuation of the diffuse emission of the ribbed tail associated with the cluster-member radio galaxy J043045.37−612335.8.

As seen in the lower panels of Fig. 13, ASKAP recovers significant diffuse emission associated with all components of the triple, with a narrow tail extending further to the north-east. At lower frequencies, the MWA images presented by Duchesne et al. (2022) show that this diffuse tail extends yet further to the north-east. The spectral index in this outermost region must be steep, as it is largely undetected by ASKAP at 943 MHz.

However, the presence of the compact radio component visible in our 2.1-GHz ATCA map would appear to be an astonishing coincidence. This compact radio component has a flux density $S_{2.1\,\mathrm{GHz}} = 0.48 \pm 0.04$ mJy, and is coincident with a galaxy (DES J043118.45−611917.9) at a photometric redshift $z_{\mathrm{phot}} = 0.722 \pm 0.129$ (Drlica-Wagner et al. 2018); if this is the core of the 'triple', then it would constitute a giant radio galaxy spanning a projected linear size of 1.03 Mpc (as posited by Rudnick et al. 2021). The compact radio component is difficult to separate from the diffuse tail seen by ASKAP at 943 MHz, though a relatively compact component is seen by ASKAP at 9-arcsec resolution; at 15-arcsec resolution, diffuse emission dominates in this region.

At 9-arcsec resolution, we measure a spectral index of $\alpha = -1.18 \pm 0.14$ between 943 MHz and 2.1 GHz for the proposed core of the triple, from the map presented in the upper right-hand panel of Fig. 13. However, this may be biased towards a steep spectrum by the diffuse emission overlaying this location. Rudnick et al. (2021) measure a peak flux density of 0.64 mJy beam^{-1} for the core, which suggests a significantly flatter core spectral index of around $\alpha \simeq -0.58$ between MeerKAT at 1.28 GHz and the ATCA at 2.1 GHz.

5.2.5 *On the nature of RG2*

The overall extent of RG2, measured from our 15-arcsec ASKAP image (lower left-hand panel of Fig. 13) is 8.7 arcmin or 608 kpc at $z = 0.0628$. Like many other tailed radio galaxies that reside in cluster environments, RG2 exhibits a complex morphology with common features like ribs and tethers (e.g. Wilber et al. 2018, 2019; Ignesti et al. 2022; Rajpurohit et al. 2022). We particularly highlight the example of the head-tail galaxy GB6 B0335+096, hosted by the galaxy cluster 2A 0335+096. LOFAR observations of this cluster presented by Ignesti et al. (2022) have revealed that the Mpc-scale tail of GB6 B0335+096 shows clumpy knotted regions along its length connected by regions of fainter diffuse emission.

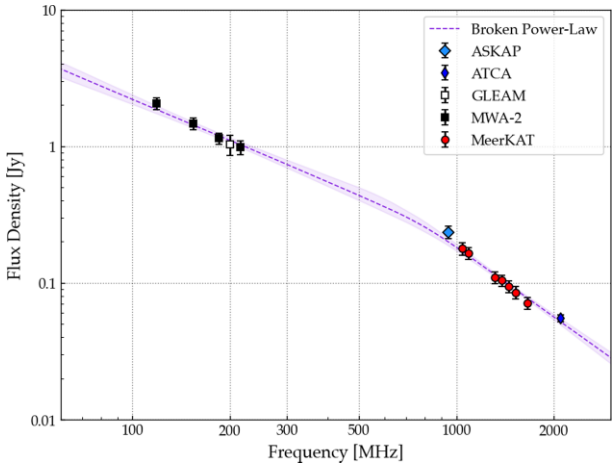

Figure 14. Spectral energy distribution (SED) for the complex tailed radio galaxy to the north-west of Abell 3266 (Source RG2; shown in Fig. 6). Our new ASKAP and ATCA measurements are shown as blue diamonds, in-band spectral measurements from the MeerKAT GCLS data are shown in red, and datapoints from the MWA from Duchesne et al. (2022) are shown as squares. Our best-fitting broken power-law spectrum is shown by the dashed violet line; the shaded region denotes the 1σ uncertainty.

These 'knots' show a flatter spectral index, and these regions likely trace instabilities between the tail and the ambient medium, being gently re-accelerated.

Overall, the similarities between the morphological and spectral properties shown by RG2 and these similar sources strongly support the interpretation that this is a single contiguous radio galaxy associated with the cluster-member galaxy J043045.37−612335.8 at $z = 0.0628$. The presence of the compact radio source 'interloper' that appears to be associated with DES J043118.45−611917.9 is curious and motivates spectroscopic follow-up, but given the available multiwavelength data we concur with the interpretation favoured by Rudnick et al. (2021), that RG2 forms a single contiguous radio galaxy, with the complex morphology – the ribs and tethers – being generated by motions in the ICM. However, the origin of the various unusual features described by Rudnick et al. (2021) are not currently understood, and further work (both observational and theoretical) is motivated.

5.3 RG5: an inclined tail?

To the north-east of Abell 3266 lies the source identified in Fig. 1 as RG5. We present a zoom on this object in Fig. 15, which shows our ASKAP and ATCA images at 9-arcsec resolution, along with the spectral index map.

5.3.1 Radio continuum properties

RG5 is another somewhat complex radio galaxy. The core appears to be associated with the cluster-member radio galaxy J043157.29−611825.8 at $z = 0.059$, which is a member of Structure 2 (Dehghan et al. 2017). Based on the optical analysis performed by Dehghan et al., Structure 2 is a radial filamentary structure with broad velocity dispersion, and has two concentrations of galaxies that are separated in redshift, suggesting a dynamically active environment.

The radio morphology of the extended jets and tails appears to support this interpretation. As is visible in Fig. 15, we detect what appear to be two jets extending from the compact (and bright) core of RG5. Both jets extend to the south-east, suggesting that this source belongs to the general 'bent-tail' class although projection effects mean we cannot determine whether this may be a head-tail, a narrow-angle tail or a wide-angle tail radio galaxy.

The jets exhibit a striking asymmetry in surface brightness: the southern jet has on average a factor of ∼4 greater surface brightness than the northern jet. This may indicate that we are seeing the jets of RG5 in projection, with the southern jet in the foreground (i.e. inclined somewhat towards us) and the northern jet in the background (i.e. inclined somewhat away from us).

Overall, each jet extends some ∼1.4 arcmin from the core (a projected distance of ∼95 kpc) before blending into the larger scale emission of what appears to be a radio lobe. Viewed in projection, we cannot determine to what extent there may be substructure in this lobe. From Fig. 15, the lobe exhibits a clear 'kink' in its morphology: some 23 arcsec (25 kpc) beyond where the jet feeds into the larger structure, the lobe abruptly bends to the north before hooking to the east once more. The cause of this sharp change in morphology is unknown; this region lies beyond the region where our *XMM–Newton* mosaic has sufficient S/N to probe the thermal properties of the ICM. Similarly, in the optical analysis of Dehghan et al. (2017), there is no obvious structure (which might trace a matter overdensity) against which the expansion of this lobe might be hindered.

5.3.2 Spectral properties

The spectral index map of RG5 is presented in the right-hand panel of Fig. 15. The core shows a typical active galaxy spectral index of $\alpha = -0.62 \pm 0.09$. While some fluctuations are visible, the jet-like structures generally show a fairly steep spectral index around $\alpha \simeq -1.3$ to -1.5 (with a typical uncertainty around 0.1); there is no clear evidence of steepening along the length of the jets. At the presumed interface where the southern jet bends to the north and feeds into the larger lobe, the spectral index is remarkably uniform with a typical value of $\langle\alpha\rangle = -1.65 \pm 0.10$. Finally, in the lobe itself, we observe a marked steepening to a median value of $\langle\alpha\rangle = -1.75 \pm 0.10$; in this region, the spectral index also appears to show increased fluctuations, perhaps indicating the mixing of different populations of electrons and/or a turbulent plasma. In places, the spectral index in the more extended lobe reaches values as steep as $\alpha = -2.2$, suggesting a particularly aged electron population.

6 CONCLUSIONS

In this paper, we have presented new, deep multiwavelength observations of the complex merging galaxy cluster Abell 3266. These observations were performed with the Australian Square Kilometre Pathfinder (ASKAP) at 943 MHz as an Early Science project for the Evolutionary Map of the Universe (EMU) survey, and combined with new dedicated observations from the Australia Telescope Compact Array (ATCA) at 2.1 GHz and re-analysis of ancillary *XMM–Newton* data to perform a highly sensitive multiwavelength study of this intriguing system.

Our observations have confirmed the presence of multiple sources of diffuse radio emission, including (i) a 'wrong-way' radio relic, (ii) an ultrasteep spectrum fossil, and (iii) an extended central diffuse 'ridge' that we are as yet unable to classify. This 'ridge' forms the brightest component of a larger scale radio halo, which is revealed for the first time in our spatially filtered ASKAP map at 943 MHz. We have performed a detailed investigation into the physical implications of these sources. Our main findings for each of the diffuse sources are as follows:

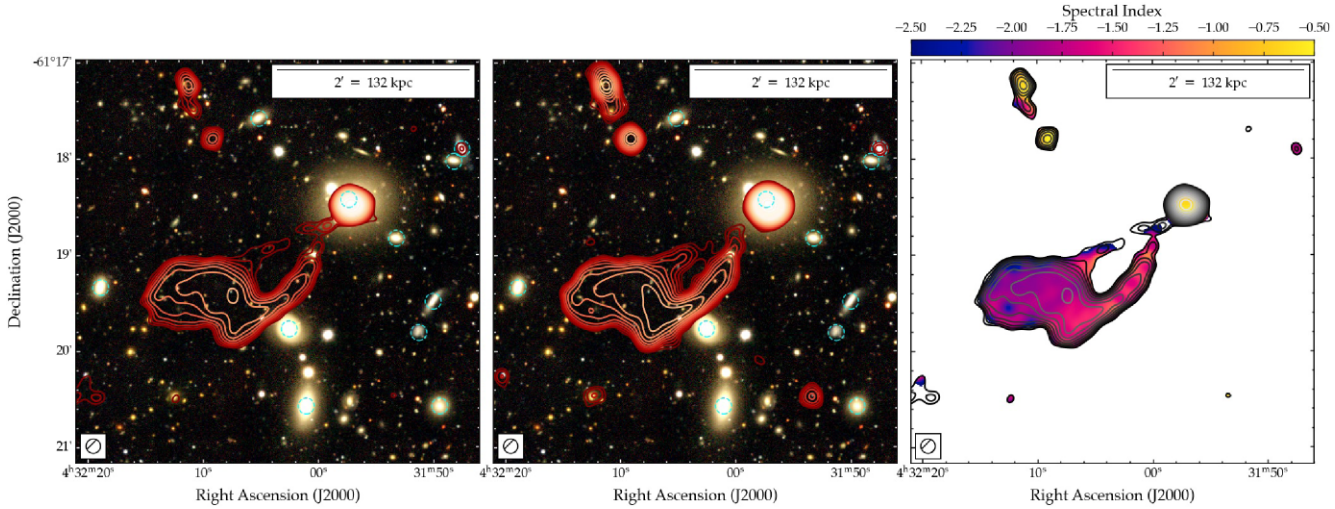

Figure 15. Images of the tailed radio galaxy to the NE of Abell 3266 (source 'RG5' in Fig. 1) at 9 arcsec resolution. The left-hand and centre panels show RGB images from DES with 943-MHz ASKAP and 2.1-GHz ATCA contours overlaid, respectively. The right-hand panel shows the radio spectral index, with ASKAP contours overlaid. All contours start at 4σ and scale by a factor of $\sqrt{2}$.

(i) *The 'wrong-way' relic* (Source D1) lies to the far south-east of the cluster centre, and is coincident with an X-ray shock detected by eROSITA. The relic has a physical size of around 579 kpc at 943 MHz, and shows a clear spectral gradient trailing towards the cluster centre. The concave nature of the relic appears contradictory, but likely reflects the complex merger history of this cluster. However, the SED shows an unambiguous spectral steepening, which strongly rejects the standard scenario of diffusive shock acceleration from the thermal pool. The extreme steepening seen in the spectrum is exceptional for a radio relic and is not trivially explained by current radio relic formation scenarios. As such, further modelling is strongly motivated, but far beyond the scope of this paper. We measure a total radio power of $P_{1.4\,\mathrm{GHz}} = (2.38 \pm 0.10) \times 10^{23}$ W Hz^{-1} for the 'wrong-way' relic in Abell 3266.

(ii) *The ultrasteep spectrum fossil* (Source D2) lies to the north-west of the cluster centre. This source, first reported by the Phase II MWA, is resolved here for the first time with ASKAP; it is undetected by the ATCA at 2.1 GHz. Using our ASKAP data in conjunction with publicly available MeerKAT data, we find clear evidence of a highly curved spectrum. The radio power of this fossil estimated from our data is $P_{1.4\,\mathrm{GHz}} = (1.36 \pm 0.13) \times 10^{22}$ W Hz^{-1}, although we note the true radio power may be lower. We identify a confirmed cluster-member galaxy as the likely original host of this source, suggesting that it is a remnant radio galaxy. No core is detected at either 943 MHz or 2.1 GHz, although the upper limit to the CP does not provide a tight constraint on the remnant nature.

(iii) *The diffuse central 'ridge'* (Source D3) is detected by ASKAP at 943 MHz but not by the ATCA at 2.1 GHz, implying an ultrasteep spectral index ($\alpha \lesssim -2.54$). We estimate an upper limit to the radio power of $P_{1.4\,\mathrm{GHz}} = (2.04 \pm 0.32) \times 10^{22}$ W Hz^{-1}. The linear extent is around 240 kpc. While we conclude that it is not a classical radio halo like those hosted by many merging clusters, its true nature is puzzling. One possibility is that it is a mini-halo candidate, in which case it would exhibit a radio power nearly two orders of magnitude below the bulk of the known population. However, Abell 3266 shows no evidence of a cool core, which would be highly unusual (but not unprecedented) for a mini-halo. Alternatively, it could represent fossil plasma from cluster-member radio galaxies that has been gently re-accelerated by the cluster merger. This steep-spectrum plasma follows the edge of the low-entropy spine seen in our *XMM–Newton* mosaic, suggesting it is bounded by this region.

(iv) We find low-surface-brightness diffuse synchrotron emission extending for a total size of up to 1.09 Mpc, confirming the presence of a *large-scale radio halo* after applying a multiresolution spatial filter to our ASKAP map at 943 MHz. We perform a point-to-point analysis at 48-arcsec resolution, finding that the radio and X-ray surface brightness are strongly correlated, with a linear slope of $b = 0.99^{+0.07}_{-0.07}$ reflecting the behaviour in the $I_\mathrm{R}/I_\mathrm{X}$ plane. From our point-to-point analysis, we also find tentative evidence of substructure, suggesting we are viewing a multicomponent radio halo or perhaps a mini-halo plus halo system. The brightest region of this radio halo is the 'ridge' – Source D3. The 'ridge' shows a superlinear slope in the $I_\mathrm{R}/I_\mathrm{X}$ plane, while the larger scale 'halo' emission shows a clearly sublinear slope. We measure an integrated flux density of $S^{\mathrm{min}}_{943\,\mathrm{MHz}} = 42.2 \pm 4.3$ and $S^{\mathrm{max}}_{943\,\mathrm{MHz}} = 67.8 \pm 6.2$ mJy, corresponding to a 1.4-GHz radio luminosity of $P^{\mathrm{min}}_{1.4\,\mathrm{GHz}} = (1.94 \pm 0.20) \times 10^{23}$ and $P^{\mathrm{max}}_{1.4\,\mathrm{GHz}} = (3.11 \pm 0.29) \times 10^{23}$ W Hz^{-1}. These luminosity values place the radio halo in Abell 3266 a factor of 4.4–7.1 below established correlations between the cluster mass and radio halo power.

Additionally, our observations also allow us to perform a detailed resolved spectral study of three of the more spectacular resolved radio galaxies hosted by Abell 3266. These include the well-known wide-angle tail radio galaxy and a complex ribbed radio galaxy recently reported by MeerKAT observations, as well as a less well-studied example to the north-east of the cluster. The spectral properties of these sources likely trace the rich dynamical history of the substructures within Abell 3266. However, further work is required to fully unpack the history of Abell 3266 and its constituent radio galaxies, and the answers to a number of questions remain elusive.

Finally, our results have demonstrated the depth and breadth of the detailed physics of cluster non-thermal phenomena and radio galaxies that can be extracted when applying next-generation techniques to exquisite multiwavelength data from the SKA Pathfinder and Precursor instruments. The coming dawn of the SKA era promises a revolution in our understanding of these rich and complex environments.

ACKNOWLEDGEMENTS

The Australia Telescope Compact Array is part of the Australia Telescope National Facility (https://ror.org/05qajvd42), which is funded by the Australian Government for operation as a National Facility managed by CSIRO. We acknowledge the Gomeroi people as the traditional owners of the site where the Australia Telescope Compact Array is located.

The Australian SKA Pathfinder is part of the Australia Telescope National Facility (https://ror.org/05qajvd42) that is managed by CSIRO. Operation of ASKAP is funded by the Australian Government with support from the National Collaborative Research Infrastructure Strategy. ASKAP uses the resources of the Pawsey Supercomputing Centre. Establishment of ASKAP, the Murchison Radio-astronomy Observatory and the Pawsey Supercomputing Centre are initiatives of the Australian Government, with support from the Government of Western Australia and the Science and Industry Endowment Fund. We acknowledge the Wajarri Yamatji people as the traditional owners of the Observatory site.

The MeerKAT Galaxy Cluster Legacy Survey (MGCLS) data products were provided by the South African Radio Astronomy Observatory and the MGCLS team and derived from observations with the MeerKAT radio telescope. The MeerKAT telescope is operated by the South African Radio Astronomy Observatory, which is a facility of the National Research Foundation, an agency of the Department of Science and Innovation.

We thank our anonymous referee for their time and their positive and constructive feedback, which has improved our paper. CJR, EB, and AB acknowledge financial support from the ERC Starting Grant 'DRANOEL', number 714245. A. Botteon acknowledges support from the VIDI research programme with project number 639.042.729, which is financed by the Netherlands Organisation for Scientific Research (NWO). KR and MB acknowledge financial support from the ERC Starting Grant 'MAGCOW', no. 714196. JMD acknowledges the support of projects PGC2018-101814-B-100 and María de Maeztu, ref. MDM-2017-0765. This research was supported by the Australian Research Council Centre of Excellence for All Sky Astrophysics in 3 Dimensions (ASTRO 3D), through project number CE170100013. LDM is supported by the ERC-StG 'ClustersXCosmo' grant agreement 716762.

This project used public archival data from the Dark Energy Survey (DES). Funding for the DES Projects has been provided by the US Department of Energy, the US National Science Foundation, the Ministry of Science and Education of Spain, the Science and Technology Facilities Council of the United Kingdom, the Higher Education Funding Council for England, the National Center for Supercomputing Applications at the University of Illinois at Urbana-Champaign, the Kavli Institute of Cosmological Physics at the University of Chicago, the Center for Cosmology and Astro-Particle Physics at the Ohio State University, the Mitchell Institute for Fundamental Physics and Astronomy at Texas A&M University, Financiadora de Estudos e Projetos, Fundação Carlos Chagas Filho de Amparo à Pesquisa do Estado do Rio de Janeiro, Conselho Nacional de Desenvolvimento Científico e Tecnológico and the Ministério da Ciência, Tecnologia e Inovação, the Deutsche Forschungsgemeinschaft, and the Collaborating Institutions in the DES.

The Collaborating Institutions are Argonne National Laboratory, the University of California at Santa Cruz, the University of Cambridge, Centro de Investigaciones Energéticas, Medioambientales y Tecnológicas-Madrid, the University of Chicago, University College London, the DES-Brazil Consortium, the University of Edinburgh, the Eidgenössische Technische Hochschule (ETH) Zürich, Fermi National Accelerator Laboratory, the University of Illinois at Urbana-Champaign, the Institut de Ciències de l'Espai (IEEC/CSIC), the Institut de Física d'Altes Energies, Lawrence Berkeley National Laboratory, the Ludwig-Maximilians Universität München and the associated Excellence Cluster Universe, the University of Michigan, the National Optical Astronomy Observatory, the University of Nottingham, The Ohio State University, the OzDES Membership Consortium, the University of Pennsylvania, the University of Portsmouth, SLAC National Accelerator Laboratory, Stanford University, the University of Sussex, and Texas A&M University.

This paper is based in part on observations at Cerro Tololo Inter-American Observatory, National Optical Astronomy Observatory, which is operated by the Association of Universities for Research in Astronomy (AURA) under a cooperative agreement with the National Science Foundation.

Finally, several PYTHON packages were used extensively during this project but are not explicitly mentioned elsewhere in this paper. We wish to acknowledge the developers of the following packages: APLPY (Robitaille & Bressert 2012), ASTROPY (Astropy Collaboration et al. 2013), CMASHER (van der Velden 2020), COLORCET (Kovesi 2015), MATPLOTLIB (Hunter 2007), NUMPY (van der Walt, Colbert & Varoquaux 2011), and SCIPY (Jones et al. 2001).

DATA AVAILABILITY

The images underlying this paper will be shared on reasonable request to the corresponding author. Raw visibilities from the ATCA are available via the Australia Telescope Online Archive (ATOA; https://atoa.atnf.csiro.au). Visibilities and pipeline-processed ASKAP images are available from CASDA (https://research.csiro.au/casda/). The *XMM–Newton* data used in this paper are available through the Science Data Archive (https://www.cosmos.esa.int/web/xmm-newton/xsa).

REFERENCES

Adam R., Goksu H., Brown S., Rudnick L., Ferrari C., 2021, A&A, 648, A60
Akamatsu H. et al., 2017, A&A, 600, A100
Astropy Collaboration et al., 2013, A&A, 558, A33
Benson B., Wittman D. M., Golovich N., Jee M. J., van Weeren R. J., Dawson W. A., 2017, ApJ, 841, 7
Bernardi G. et al., 2016, MNRAS, 456, 1259
Biava N. et al., 2021, MNRAS , 508, 3995
Blandford R., Eichler D., 1987, Phys. Rep., 154, 1
Blasi P., Colafrancesco S., 1999, Astropart. Phys., 12, 169
Bonafede A. et al., 2012, MNRAS, 426, 40
Bonnassieux E., Tasse C., Smirnov O., Zarka P., 2018, A&A, 615, A66
Boschin W., Girardi M., Barrena R., 2012, A&A, 547, A44
Botteon A., Gastaldello F., Brunetti G., Dallacasa D., 2016a, MNRAS, 460, L84
Botteon A., Gastaldello F., Brunetti G., Kale R., 2016b, MNRAS, 463, 1534
Botteon A., Gastaldello F., Brunetti G., 2018, MNRAS, 476, 5591
Botteon A. et al., 2020a, MNRAS, 499, L11
Botteon A., Brunetti G., Ryu D., Roh S., 2020b, A&A, 634, A64
Botteon A. et al., 2020c, ApJ, 897, 93
Botteon A. et al., 2021, ApJ, 914, L29
Brienza M. et al., 2016, A&A, 585, A29
Brienza M. et al., 2017, A&A, 606, A98
Brienza M. et al., 2021, Nat. Astron., 5, 1261
Brienza M. et al., 2022, A&A, 661, A92
Briggs D. S., 1995, PhD Thesis, The New Mexico Institute of Mining and Technology
Brüggen M. et al., 2021, A&A, 647, A3
Brunetti G., Jones T. W., 2014, Int. J. Mod. Phys. D, 23, 1430007

Brunetti G., Setti G., Feretti L., Giovannini G., 2001, MNRAS, 320, 365
Brunetti G. et al., 2008, Nature, 455, 944
Bruno L. et al., 2021, A&A, 650, A44
Burns J. O., 1998, Science, 280, 400
Cantwell T. M., Scaife A. M. M., Oozeer N., Wen Z. L., Han J. L., 2016, MNRAS, 458, 1803
Cassano R. et al., 2013, ApJ, 777, 141
Chapman J. M., Dempsey J., Miller D., Heywood I., Pritchard J., Sangster E., Whiting M., Dart M., 2017, in Lorente N. P. F., Shortridge K., Wayth R., eds, ASP Conf. Ser. Vol. 512, Astronomical Data Analysis Software and Systems XXV. Astron. Soc. Pac., San Francisco, p. 73
Dallacasa D. et al., 2009, ApJ, 699, 1288
de Gasperin F. et al., 2017, Sci. Adv., 3, e1701634
de Gasperin F. et al., 2022, A&A, 659, A146
De Grandi S., Molendi S., 1999, ApJ, 527, L25
de Ruiter H. R., Parma P., Fanti C., Fanti R., 1990, A&A, 227, 351
DeBoer D. R. et al., 2009, Proc. IEEE, 97, 1507
Dehghan S., 2014, PhD Thesis, Victoria Univ. Wellington
Dehghan S., Johnston-Hollitt M., Colless M., Miller R., 2017, MNRAS, 468, 2645
Dennison B., 1980, ApJ, 239, L93
DES Collaboration et al., 2021, ApJS, 255, 20
Di Gennaro G. et al., 2018, ApJ, 865, 24
Di Mascolo L. et al., 2021, A&A, 650, A153
Dominguez-Fernandez P., Bruggen M., Vazza F., Banda-Barragan W. E., Rajpurohit K., Mignone A., Mukherjee D., Vaidya B., 2021, MNRAS, 500, 795
Drlica-Wagner A. et al., 2018, ApJS, 235, 33
Duchesne S. W., Johnston-Hollitt M., 2019, Publ. Astron. Soc. Aust., 36, e016
Duchesne S. W., Johnston-Hollitt M., Bartalucci I., Hodgson T., Pratt G. W., 2021a, Publ. Astron. Soc. Aust., 38, e005
Duchesne S. W., Johnston-Hollitt M., Offringa A. R., Pratt G. W., Zheng Q., Dehghan S., 2021b, Publ. Astron. Soc. Aust., 38, e010
Duchesne S. W., Johnston-Hollitt M., Wilber A. G., 2021c, Publ. Astron. Soc. Aust., 38, e031
Duchesne S. W., Johnston-Hollitt M., Bartalucci I., 2021d, Publ. Astron. Soc. Aust., 38, e053
Duchesne S. W., Johnston-Hollitt M., Riseley C. J., Bartalucci I., Keel S. R., 2022, MNRAS, 511, 3525
Eckert D., Ettori S., Pointecouteau E., Molendi S., Paltani S., Tchernin C., 2017, Astron. Nachr., 338, 293
Ensslin T. A., Biermann P. L., Klein U., Kohle S., 1998, A&A, 332, 395
Feretti L., Fusco-Femiano R., Giovannini G., Govoni F., 2001, A&A, 373, 106
Ferrari C., Govoni F., Schindler S., Bykov A. M., Rephaeli Y., 2008, Space Sci. Rev., 134, 93
Finoguenov A., Henriksen M. J., Miniati F., Briel U. G., Jones C., 2006, ApJ, 643, 790
Finoguenov A., Sarazin C. L., Nakazawa K., Wik D. R., Clarke T. E., 2010, ApJ, 715, 1143
Fleenor M. C., Rose J. A., Christiansen W. A., Hunstead R. W., Johnston-Hollitt M., Drinkwater M. J., Saunders W., 2005, AJ, 130, 957
Foreman-Mackey D., Hogg D. W., Lang D., Goodman J., 2013, PASP, 125, 306
Frater R. H., Brooks J. W., Whiteoak J. B., 1992, J. Electr. Electron. Eng. Aust., 12, 103
Gendron-Marsolais M. et al., 2020, MNRAS, 499, 5791
Gendron-Marsolais M. L. et al., 2021, ApJ, 911, 56
Ghirardini V. et al., 2019, A&A, 621, A41
Giacintucci S. et al., 2005, A&A, 440, 867
Giacintucci S., Markevitch M., Cassano R., Venturi T., Clarke T. E., Brunetti G., 2017, ApJ, 841, 71
Giacintucci S., Markevitch M., Cassano R., Venturi T., Clarke T. E., Kale R., Cuciti V., 2019, ApJ, 880, 70
Giovannini G., Feretti L., Gregorini L., Parma P., 1988, A&A, 199, 73
Giovannini G., Bonafede A., Feretti L., Govoni F., Murgia M., Ferrari F., Monti G., 2009, A&A, 507, 1257
Gitti M., Brunetti G., Setti G., 2002, A&A, 386, 456
Godfrey L. E. H., Morganti R., Brienza M., 2017, MNRAS, 471, 891
Goodman J., Weare J., 2010, Commun. Appl. Math. Comput. Sci., 5, 65
Govoni F., Enßlin T. A., Feretti L., Giovannini G., 2001a, A&A, 369, 441
Govoni F., Feretti L., Giovannini G., Böhringer H., Reiprich T. H., Murgia M., 2001b, A&A, 376, 803
Govoni F., Murgia M., Markevitch M., Feretti L., Giovannini G., Taylor G. B., Carretti E., 2009, A&A, 499, 371
Govoni F. et al., 2019, Science, 364, 981
Guzman J. et al., 2019, Astrophysics Source Code Library, record ascl:1912.003
Harwood J. J., Hardcastle M. J., Croston J. H., Goodger J. L., 2013, MNRAS, 435, 3353
Harwood J. J., Hardcastle M. J., Croston J. H., 2015, MNRAS, 454, 3403
Henriksen M. J., Tittley E. R., 2002, ApJ, 577, 701
Henriksen M., Donnelly R. H., Davis D. S., 2000, ApJ, 529, 692
Hoang D. N. et al., 2019, A&A, 622, A20
Hoang D. N. et al., 2021, A&A, 656, A154
Hodgson T., Bartalucci I., Johnston-Hollitt M., McKinley B., Vazza F., Wittor D., 2021, ApJ, 909, 198
Hoeft M., Brüggen M., 2007, MNRAS, 375, 77
Hong S. E., Kang H., Ryu D., 2015, ApJ, 812, 49
Hotan A. W. et al., 2014, Publ. Astron. Soc. Aust., 31, e041
Hotan A. W. et al., 2021, Publ. Astron. Soc. Aust., 38, e009
Hunter J. D., 2007, Comput. Sci. Eng., 9, 90
Hurley-Walker N. et al., 2017, MNRAS, 464, 1146
Huynh M., Dempsey J., Whiting M. T., Ophel M., 2020, in Ballester P., Ibsen J., Solar M., Shortridge K., eds, ASP Conf. Ser. Vol. 522, Astronomical Data Analysis Software and Systems XXVII. Astron. Soc. Pac., San Francisco, p. 263
HyeongHan K. et al., 2020, ApJ, 900, 127
Ignesti A., Brunetti G., Gitti M., Giacintucci S., 2020a, A&A, 640, A37
Ignesti A. et al., 2020b, A&A, 643, A172
Ignesti A. et al., 2022, A&A, 659, A20
Inchingolo G., Wittor D., Rajpurohit K., Vazza F., 2022, MNRAS, 509, 1160
Jaffe W. J., Perola G. C., 1973, A&A, 26, 423
Johnston S. et al., 2007, Publ. Astron. Soc. Aust., 24, 174
Johnston-Hollitt M., Dehghan S., Pratley L., 2015, Proc. Sci., Advancing Astrophysics with the Square Kilometre Array (AASKA14). SISSA, Trieste, PoS#101
Jones E. et al., 2001, SciPy: Open Source Scientific Tools for Python. Available at: http://www.scipy.org/
Jones A. et al., 2021, MNRAS, 505, 4762
Jurlin N., Brienza M., Morganti R., Wadadekar Y., Ishwara-Chandra C. H., Maddox N., Mahatma V., 2021, A&A, 653, A110
Kale R., Shende K. M., Parekh V., 2019, MNRAS, 486, L80
Kang H., 2021, J. Kor. Astron. Soc., 54, 103
Kang H., Ryu D., 2011, ApJ, 734, 18
Kang H., Ryu D., 2016, ApJ, 823, 13
Kardashev N. S., 1962, SvA, 6, 317
Kelly B. C., 2007, ApJ, 665, 1489
Knowles K. et al., 2016, MNRAS, 459, 4240
Knowles K. et al., 2022, A&A, 657, A56
Komissarov S. S., Gubanov A. G., 1994, A&A, 285, 27
Kovesi P., 2015, preprint (arXiv:1509.03700)
Lal D. V., 2020, AJ, 160, 161
Locatelli N. T. et al., 2020, MNRAS, 496, L48
Loi F. et al., 2020, MNRAS, 498, 1628
McConnell D. et al., 2016, Publ. Astron. Soc. Aust., 33, e042
Mahatma V. H. et al., 2018, MNRAS, 475, 4557
Mandal S. et al., 2020, A&A, 634, A4
Markevitch M., Forman W. R., Sarazin C. L., Vikhlinin A., 1998, ApJ, 503, 77
Mohr J. J., Mathiesen B., Evrard A. E., 1999, ApJ, 517, 627
Murgia M. et al., 2011, A&A, 526, A148
Murphy T., 1999, Honours Thesis, Univ. Sydney

Murphy T., Hunstead R. W., 2002, in Pramesh Rao A., Swarup G., Gopal-Krishna, eds, Proc. IAU Symp. 199, The Universe at Low Radio Frequencies. Kluwer, Dordrecht, p. 151
Norris R. P. et al., 2011, Publ. Astron. Soc. Aust., 28, 215
Norris R. P. et al., 2021, Publ. Astron. Soc. Aust., 38, e046
Owen F. N., Rudnick L., Eilek J., Rau U., Bhatnagar S., Kogan L., 2014, ApJ, 794, 24
Pacholczyk A. G., 1970, Radio Astrophysics. Nonthermal Processes in Galactic and Extragalactic Sources. Freeman, San Fransisco
Parekh V. et al., 2022, MNRAS, 509, 3086
Petrosian V., 2001, ApJ, 557, 560
Pfrommer C., Enßlin T. A., 2004, A&A, 413, 17
Planck Collaboration XXVII, 2016, A&A, 594, A27
Pratley L., Johnston-Hollitt M., Dehghan S., Sun M., 2013, MNRAS, 432, 243
Pratt G. W., Arnaud M., 2002, A&A, 394, 375
Predehl P. et al., 2021, A&A, 647, A1
Quici B. et al., 2021, Publ. Astron. Soc. Aust., 38, e008
Quici B., Turner R. J., Seymour N., Hurley-Walker N., Shabala S. S., Ishwara-Chandra C. H., 2022, MNRAS, 514, 3466
Quintana H., Ramirez A., Way M. J., 1996, AJ, 112, 36
Raja R. et al., 2020, MNRAS, 493, L28
Rajpurohit K. et al., 2018, ApJ, 852, 65
Rajpurohit K. et al., 2020, A&A, 636, A30
Rajpurohit K. et al., 2021a, A&A, 646, A135
Rajpurohit K. et al., 2021b, A&A, 654, A41
Rajpurohit K. et al., 2022, ApJ, 927, 80
Randriamanakoto Z., Ishwara-Chandra C. H., Taylor A. R., 2020, MNRAS, 496, 3381
Reid A. D., 1999, PhD Thesis, Univ. Sydney
Riseley C. J., 2016, PhD Thesis, Univ. Southampton
Riseley C. J., Scaife A. M. M., Oozeer N., Magnus L., Wise M. W., 2015, MNRAS, 447, 1895
Riseley C. J. et al., 2022, MNRAS, 512, 4210
Robitaille T., Bressert E., 2012, Astrophysics Source Code Library, record ascl:1208.017
Roettiger K., Burns J. O., Stone J. M., 1999, ApJ, 518, 603
Rudnick L., 2002a, New Astron. Rev., 46, 101
Rudnick L., 2002b, PASP, 114, 427
Rudnick L., Cotton W., Knowles K., Kolokythas K., 2021, Galaxies, 9, 81
Sanders J. S. et al., 2022, A&A, 661, A36
Sault R. J., Teuben P. J., Wright M. C. H., 1995, in Shaw R. A., Payne H. E., Hayes J. J. E., eds, ASP Conf. Ser. Vol. 77, Astronomical Data Analysis Software and Systems IV. Astron. Soc. Pac., San Francisco, p. 433
Sauvageot J. L., Belsole E., Pratt G. W., 2005, A&A, 444, 673
Savini F. et al., 2018, MNRAS, 478, 2234
Savini F. et al., 2019, A&A, 622, A24
Shimwell T. W., Brown S., Feain I. J., Feretti L., Gaensler B. M., Lage C., 2014, MNRAS, 440, 2901
Shimwell T. W., Markevitch M., Brown S., Feretti L., Gaensler B. M., Johnston-Hollitt M., Lage C., Srinivasan R., 2015, MNRAS, 449, 1486
Shweta A., Athreya R., Sekhar S., 2020, ApJ, 897, 115
Skillman S. W., Xu H., Hallman E. J., O'Shea B. W., Burns J. O., Li H., Collins D. C., Norman M. L., 2013, ApJ, 765, 21
Smirnov O. M., Tasse C., 2015, MNRAS, 449, 2668
Snowden S. L., Mushotzky R. F., Kuntz K. D., Davis D. S., 2008, A&A, 478, 615
Stuardi C. et al., 2019, MNRAS, 489, 3905
Tasse C., 2014, A&A, 566, A127
Tasse C. et al., 2018, A&A, 611, A87
Timmerman R., van Weeren R. J., McDonald M., Ignesti A., McNamara B. R., Hlavacek-Larrondo J., Röttgering H. J. A., 2021, A&A, 646, A38
Tingay S. J. et al., 2013, Publ. Astron. Soc. Aust., 30, e007
Trasatti M., Akamatsu H., Lovisari L., Klein U., Bonafede A., Brüggen M., Dallacasa D., Clarke T., 2015, A&A, 575, A45
Turner R. J., 2018, MNRAS, 476, 2522
Turner R. J., Rogers J. G., Shabala S. S., Krause M. G. H., 2018, MNRAS, 473, 4179
Urdampilleta I., Akamatsu H., Mernier F., Kaastra J. S., de Plaa J., Ohashi T., Ishisaki Y., Kawahara H., 2018, A&A, 618, A74
van Haarlem M. P. et al., 2013, A&A, 556, A2
van Weeren R. J. et al., 2017a, Nat. Astron., 1, 0005
van Weeren R. J. et al., 2017b, ApJ, 835, 197
van Weeren R. J., de Gasperin F., Akamatsu H., Brüggen M., Feretti L., Kang H., Stroe A., Zandanel F., 2019, Space Sci. Rev., 215, 16
van der Velden E., 2020, J. Open Source Softw., 5, 2004
van der Walt S., Colbert S. C., Varoquaux G., 2011, Comput. Sci. Eng., 13, 22
Venturi T. et al., 2017, A&A, 603, A125
Venturi T. et al., 2022, A&A, 660, A81
Wang Q. H. S., Markevitch M., 2018, ApJ, 868, 45
Wayth R. B. et al., 2015, Publ. Astron. Soc. Aust., 32, e025
Wayth R. B. et al., 2018, Publ. Astron. Soc. Aust., 35, e033
Wilber A. et al., 2018, MNRAS, 473, 3536
Wilber A. et al., 2019, A&A, 622, A25
Wilber A. G., Johnston-Hollitt M., Duchesne S. W., Tasse C., Akamatsu H., Intema H., Hodgson T., 2020, Publ. Astron. Soc. Aust., 37, e040
Wilson W. E. et al., 2011, MNRAS, 416, 832
Wittor D., Ettori S., Vazza F., Rajpurohit K., Hoeft M., Domínguez-Fernández P., 2021, MNRAS, 506, 396
Xi S.-Q., Wang X.-Y., Liang Y.-F., Peng F.-K., Yang R.-Z., Liu R.-Y., 2018, Phys. Rev. D, 98, 063006
ZuHone J. A., Markevitch M., Brunetti G., Giacintucci S., 2013, ApJ, 762, 78
ZuHone J. A., Brunetti G., Giacintucci S., Markevitch M., 2015, ApJ, 801, 146

SUPPORTING INFORMATION

Supplementary data are available at *MNRAS* online.

Figure A1. ATCA images of Abell 3266 produced using standard techniques in MIRIAD (left-hand panel) and using third-generation calibration techniques using DDFACET and KILLMS (right-hand panel). Images are shown at 6-arcsec resolution and on matching colour scales, ranging between -3σ and 200σ, where $\sigma = 14.5$ μJy beam^{-1} is the rms noise in our DDFACET image.

Figure A2. ASKAP images of Abell 3266 produced by ASKAPSOFT (left-hand panel) and with further post-processing using DDFACET and KILLMS (right-hand panel). Images are shown at 15.5 × 13.7 arcsec^2 resolution and on matching colour scales, ranging between -3σ and 200σ, where $\sigma = 36.7$ μJy beam^{-1} is the rms noise in our DDFACET image.

Please note: Oxford University Press is not responsible for the content or functionality of any supporting materials supplied by the authors. Any queries (other than missing material) should be directed to the corresponding author for the article.

[1]*Dipartimento di Fisica e Astronomia, Università degli Studi di Bologna, via P. Gobetti 93/2, I-40129 Bologna, Italy*
[2]*INAF – Istituto di Radioastronomia, via P. Gobetti 101, I-40129 Bologna, Italy*
[3]*CSIRO Space and Astronomy, PO Box 1130, Bentley, WA 6102, Australia*
[4]*ICRAR, The University of Western Australia, 35 Stirling Hw, 6009 Crawley, Australia*
[5]*International Centre for Radio Astronomy Research, Curtin University, Bentley, WA 6102, Australia*
[6]*The University of Melbourne, School of Physics, Parkville, VIC 3010, Australia*
[7]*ARC Centre of Excellence for All Sky Astrophysics in 3 Dimensions (ASTRO 3D)*
[8]*CSIRO Space and Astronomy, PO Box 76, Epping, NSW 1710, Australia*

[9]*Leiden Observatory, Leiden University, PO Box 9513, NL-2300 RA Leiden, the Netherlands*
[10]*Minnesota Institute for Astrophysics, University of Minnesota, 116 Church St SE, Minneapolis, MN 55455, USA*
[11]*Thüringer Landessternwarte, Sternwarte 5, D-07778 Tautenburg, Germany*
[12]*Department of Astronomy, University of Geneva, Ch. d'Ecogia 16, CH-1290 Versoix, Switzerland*
[13]*GEPI and USN, Observatoire de Paris, CNRS, Universite Paris Diderot, 5 place Jules Janssen, F-92190 Meudon, France*
[14]*Centre for Radio Astronomy Techniques and Technologies, Department of Physics and Electronics, Rhodes University, Grahamstown 6140, South Africa*
[15]*The Inter-University Institute for Data Intensive Astronomy (IDIA), Department of Astronomy, University of Cape Town, Private Bag X3, Rondebosch, 7701, South Africa*
[16]*School of Science, Western Sydney University, Locked Bag 1797, Penrith, NSW 2751, Australia*
[17]*Instituto de Fisica de Cantabria, CSIC-Universidad de Cantabria, E-39005 Santander, Spain*
[18]*Astronomy Unit, Department of Physics, University of Trieste, via Tiepolo 11, I-34131 Trieste, Italy*
[19]*INAF – Osservatorio Astronomico di Trieste, via Tiepolo 11, I-34131 Trieste, Italy*
[20]*IFPU – Institute for Fundamental Physics of the Universe, Via Beirut 2, I-34014 Trieste, Italy*
[21]*Australian Astronomical Optics, Macquarie University, 105 Delhi Rd, North Ryde, NSW 2113, Australia*
[22]*Curtin Institute for Computation, Curtin University, GPO Box U1987, Perth, WA 6845, Australia*
[23]*Argelander-Institut für Astronomie, Universität Bonn, Auf dem Hügel 71, D-53121 Bonn, Germany*

This paper has been typeset from a TEX/LATEX file prepared by the author.